February 1, 2023

STATUS REPORT OF THE AD-3 ASACUSA COLLABORATION

Progress in 2022 and plans for 2023

CERN-SPSC-2023-007 / SPSC-SR-323
01/02/2023

ASACUSA collaboration

C. Amsler[a], D. Barna[b], H. Breuker[c], M. Bumbar[a], S. Chesnevskaya[a], G. Costantini[d], R. Ferragut[e], M. Giammarchi[f], A. Gligorova[a], G. Gosta[d], H. Higaki[g], M. Hori[h,i,j*], E. D. Hunter[a], C. Killian[a], V. Kraxberger[a], N. Kuroda[l], A. Lanz[a], M. Leali[d], G. Maero[m], C. Malbrunot[n1], V. Mascagna[d], Y. Matsuda[l], V. Mäckel[a2], S. Migliorati[d], D. J. Murtagh[a], A. Nanda[a], L. Nowak[a,n], F. Parnefjord Gustafsson[a,n], S. Rheinfrank[a], M. Romé[m], M. C. Simon[a], M. Tajima[k], V. Toso[e], U. Uggerhøj[o], S. Ulmer[c], L. Venturelli[d], A. Weiser[a], E. Widmann[a*], T. Wolz[n], Y. Yamazaki[c], J. Zmeskal[a]

[a]Stefan Meyer Institute, [b]Wigner Research Centre for Physics, [c]Ulmer Fundamental Symmetries Laboratory, RIKEN, [d]Dipartimento di Ingegneria dell'Informazione, Università degli Studi di Brescia and INFN Pavia, [e]Politechnico di Milano, [f]INFN Milano, [g]Graduate School of Advanced Sciences of Matter, Hiroshima University, [h]QUANTUM Institut für Physik, Johannes Gutenberg-Universität Mainz, [i]Max-Planck-Institut für Quantenoptik, [j]Imperial College London, [k]Nishina Center for Accelerator-Based Science, RIKEN, [l]Institute of Physics, the University of Tokyo, [m]Dipartimento di Fisica, Università degli Studi di Milano and INFN Milano, [n]Experimental Physics Department, CERN, [o]Department of Physics and Astronomy, Aarhus University
* Co-spokespersons

[1]present address: TRIUMF, Vancouver, Canada
[2]present address: INFICON GmbH, Köln

Executive summary

In 2022 the ASACUSA collaboration published a major paper [1] that described the surprising phenomenon that antiprotonic helium atoms embedded in superfluid helium showed visible-wavelength spectral lines that are narrower than those of many other implanted normal-matter atoms. At the superfluid phase transition temperature, the spectral linewidth abruptly narrowed to sub-GHz linewidths corresponding to a relative spectral resolution of 2×10^{-6}. This result implies that other exotic helium atoms containing antideuterons, or negatively-charged mesons and hyperons may be similarly measured with a high spectral resolution in He-II. This is relevant for achieving high precision measurements in the laser spectroscopy experiment of pionic helium atoms ($\pi^4\mathrm{He}^+$) at the 590 MeV cyclotron facility of PSI [2–4]. The fact that the lineshapes are so sensitive to the liquid temperature and phase may indicate that $\overline{p}\mathrm{He}^+$ could be used as a probe to study some condensed matter effects in He-II.

The collaboration successfully carried out **laser spectroscopy of a known laser resonance of antiprotonic helium using the ELENA beam**. The hyperfine structure of this resonance was resolved. Numerous issues were identified with the experimental beamline, most seriously the high load of helium gas entering into ELENA. The beamline will be suitably modified in 2023.

We continued refurbishing the traps of the *antihydrogen hyperfine spectroscopy* experiment located at the LNE05 beam line to enable a higher production rate of antihydrogen and an efficient operation during the ELENA era. Remaining tasks were the upgrade of the control system of our antiproton catching trap MUSASHI and the replacement of our positron system to remove a superconducting magnet needing several dewars of liquid helium per week.

The cycle time of MUSASHI was reduced to less than one AD cycle, increasing the antiproton beam production rate significantly. Optimisation of the beam optics from ELENA has allowed to trap and cool more than one million $\overline{\mathrm{p}}$ per ELENA shot, but the beam shape is still not optimal. Further optimisation planned for 2023 may lead to a even larger number of trapped $\overline{\mathrm{p}}$. Antiprotons were transferred to the Cusp mixing trap, where $> 2 \times 10^5\,\overline{\mathrm{p}}$ could be trapped and compressed.

The installation of a commercial First Point Scientific positron system previously used at Aarhus University turned out to be very time consuming due to multiple pieces of damage that occurred during transport. At the end of the year positrons could be trapped albeit at a much lower rate than obtained previously at Aarhus, which still needs to be improved before the beam time 2023. An accumulator was commissioned which will allow to accumulate e^+ outside the Cusp trap improving the vacuum conditions during mixing. Still missing is a new ^{22}Na source whose delivery is delayed by > 6 months and which is indispensable to generate enough positrons for antihydrogen experiments. Once enough positrons become available, mixing can commence with low-temperature high-density plasmas as demonstrated in 2021 with electrons. The sextupole magnet and microwave cavity have been recommissioned or characterised, resp., so that first interactions of microwave with an antihydrogen beam can commence towards the end of the 2023 beam time.

The beam steering elements needed to generate a slow extracted $\overline{\mathrm{p}}$ beam from MUSASHI for *annihilation studies* has been designed and will be installed before the beam time 2023. This will be done in a way that switching between antiproton transfer for antihydrogen production and slow extraction can be done without vacuum intervention, enabling flexible scheduling. The experiment aims at providing bench mark data on pion and heavy fragment multiplicities and energy deposit of charged annihilation products for Monte Carlo codes used by all collaborations at AD/ELENA.

Data taking previously have been analysed, and simulations are under way for an improved setup using Timepix4 detectors.

A *hydrogen beam* used to characterise the microwave cavity has been removed from CERN after the optimum conditions for in-beam hyperfine spectroscopy of antihydrogen were obtained. An experiment to determine SME coefficients using this beam was finished and is currently in the final state of analysis. A second installation producing an excited hydrogen beam to study schemes for deexcitation of Rydberg antihydrogen as generated during mixing is still in operation at CERN, in cooperation with AEgIS.

Contents

I Antiprotonic Helium **1**

1 Observation of narrow spectral lines of antiprotonic helium atoms embedded in superfluid helium **1**
1.1 Anomalous spectral narrowing effect . . . 3
1.2 Spectral shifts . . . 5
1.3 Discussion . . . 5

2 Laser spectroscopy of antiprotonic helium atoms using ELENA **5**
2.1 Beamline upgrades . . . 5
2.2 Observation of laser resonance . . . 8
2.3 Helium accumulation in ELENA . . . 8

3 Reorientation of the collaboration **9**

4 Improved MD-RIA calculations of antiproton transmission through polymer foils **10**

5 Induction decelerator **12**

6 Preparations for the 2023 beamtime **13**

II Antihydrogen **14**

7 Antiprotons **15**
7.1 Antiproton trapping in MUSASHI . . . 15
7.2 Antiproton trapping in the Cusp . . . 16
7.3 Scintillating bar detector . . . 17

8 Positrons **18**
8.1 Positron trap . . . 19
8.2 Positron accumulator . . . 21

9 Spectroscopy apparatus **22**
9.1 Sextupole focusing magnet . . . 22
9.2 Antihydrogen detector . . . 22

10 Plans for 2023 **25**

III Study of annihilations with slow extracted antiprotons **26**

1 Introduction **26**
1.1 Design and construction of beam optics elements for the transport of slow extracted antiprotons 26

2 Detector development **28**
2.1 Geant4 simulations . . . 28
2.2 Timepix4 measurements with heavy ions . . . 30

3 Plans for 2023 **30**

IV Experiments with hydrogen beams **31**

1 Commissioning of ASACUSAs hyperfine spectrometer **31**

2 Hydrogen hyperfine spectroscopy at magnetic fields close to 1 mT **32**

3 Excited hydrogen beam **34**

4 Plans for 2023 **35**

References **37**

Part I
Antiprotonic Helium

1 Observation of narrow spectral lines of antiprotonic helium atoms embedded in superfluid helium

When atoms are placed into liquids, their optical spectral lines corresponding to the transitions of the atomic electron are greatly broadened compared to those of atoms that are isolated in vacuum. In 2022 the ASACUSA collaboration published a major paper [1] that described the surprising phenomenon that $\overline{p}^4\mathrm{He}^+$ atoms [5–21] embedded in superfluid helium (He-II) showed visible-wavelength spectral lines that are narrower than those of many other implanted normal-matter atoms. At the superfluid phase transition temperature, the spectral linewidth abruptly narrowed to sub-GHz linewidths corresponding to a relative spectral resolution of 2×10^{-6}. This is more than a factor of 10 narrower than the $\overline{p}^4\mathrm{He}^+$ spectra observed in supercritical helium targets of lower density. This result implies that other exotic helium atoms containing antideuterons, or negatively-charged mesons and hyperons may be similarly measured with a high spectral resolution in He-II. This is relevant for achieving high precision measurements in the laser spectroscopy experiment of pionic helium atoms ($\pi^4\mathrm{He}^+$) at the 590 MeV cyclotron facility of PSI [2–4]. The fact that the lineshapes are so sensitive to the liquid temperature and phase may indicate that $\overline{p}\mathrm{He}^+$ could be used as a probe to study some condensed matter effects in He-II. The results produced some interest in the field.

Past ASACUSA results showed that the highly excited $n > 41$ antiproton orbitals of $\overline{p}^4\mathrm{He}^+$ atoms that extend outside the 1s electron shell with a root-mean-square radius $r_e \approx 40$ pm are

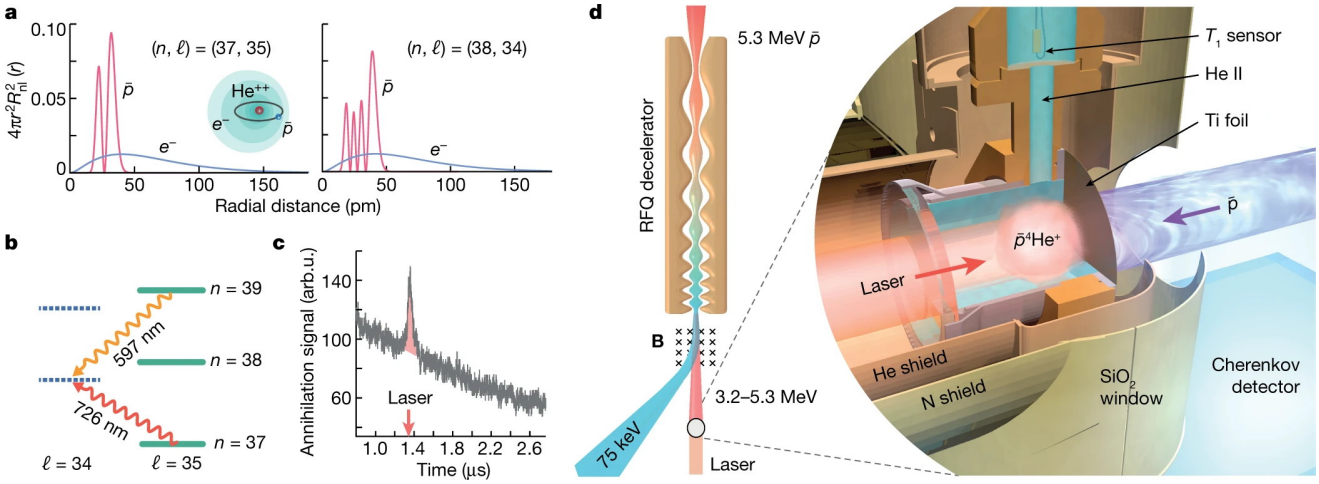

Figure 1 – Radial distribution functions of the antiproton (indicated by red curves) and electron (blue curves) for states $(n, \ell) = (37, 35)$ and $(38, 34)$ of a single isolated $\overline{p}^4\mathrm{He}^+$ atom (a). $R_{n,\ell}(r)$ denotes the radial component of the antiproton or electron orbital at a distance r from the helium nucleus. Laser transitions between the two states involve an extremely small ($\Delta r_e \leq 2$ pm) change in the root-mean-square radius of the orbital of the 1s electron. b, Energy level diagram of $\overline{p}^4\mathrm{He}^+$ indicating the positions of the transitions $(37, 35) \rightarrow (38, 34)$ and $(39, 35) \rightarrow (38, 34)$. c, Signal of the Cherenkov detector with the laser resonance induced at $t \approx 1.4\mu$s after $\overline{p}^4\mathrm{He}^+$ formation. d, Experimental layout. From Ref. [1].

destroyed in atomic collisions so that no laser resonance could be detected [22]. The $n = 30 - 40$ orbitals, on the other hand, lie well within the electron shell (see Fig. 1A) and so should be better protected, but numerous states were found to likewise be destroyed [23–25] for atoms synthesized in gas targets of atomic density $\rho = 10^{20} - 10^{21}$ cm^{-3}. Laser spectroscopy of antiprotonic atoms suspended in liquid targets had therefore not been achieved before.

In the work published in 2022 [1], two laser transitions $(n, \ell) = (37, 35) \rightarrow (38, 34)$ and $(39, 35) \rightarrow (38, 34)$ at the respective wavelengths $\lambda = 726$ nm and 597 nm were detected for antiprotonic atoms submerged in liquid helium targets. The parent states $(37, 35)$ and $(39, 35)$ of the resonances have microsecond-scale lifetimes, whereas the daughter state $(38, 34)$ has an Auger width [26, 27] of 21 MHz (see energy level diagram of Fig. 1B). The radius of a single isolated $\overline{p}\mathrm{He}^+$ atom is smaller by an order of magnitude (Fig. 1A) compared to the valance orbitals of the other impurity atoms such as alkaline, alkaline earth, and lanthanide atoms. The optical transitions of the massive antiproton moreover involve extremely small changes in the radius $\Delta r_e \leq 2$ pm of the electron and the related $\overline{p}^4\mathrm{He}^+$-He pairwise potentials. For all these reasons, we may expect lineshapes that are quantitatively different from many other atoms.

The 726 nm transition with a dipole moment $d_m = 0.018$ a.u. was excited by irradiating the atoms with a 50 ns long laser pulse with a linewidth of 60 MHz and fluence of $\varepsilon = 4$ mJ·cm^{-2} (Fig. 1B) that was generated by a Ti:sapphire pulsed laser injection-seeded by a continuous-wave laser [28]. The 597 nm resonance that had a larger dipole moment $d_m = 0.24$ a.u. was excited by a laser pulse with a linewidth of 80 MHz and fluence $\varepsilon = 0.12$ mJ·cm^{-2}. The laser pulse was generated by a cw pulse-amplified dye laser. The frequencies of the seed lasers were measured with a femtosecond frequency comb. A mechanical shutter prevented the seed laser beam from entering and heating up the target during the intervals between the antiproton arrivals.

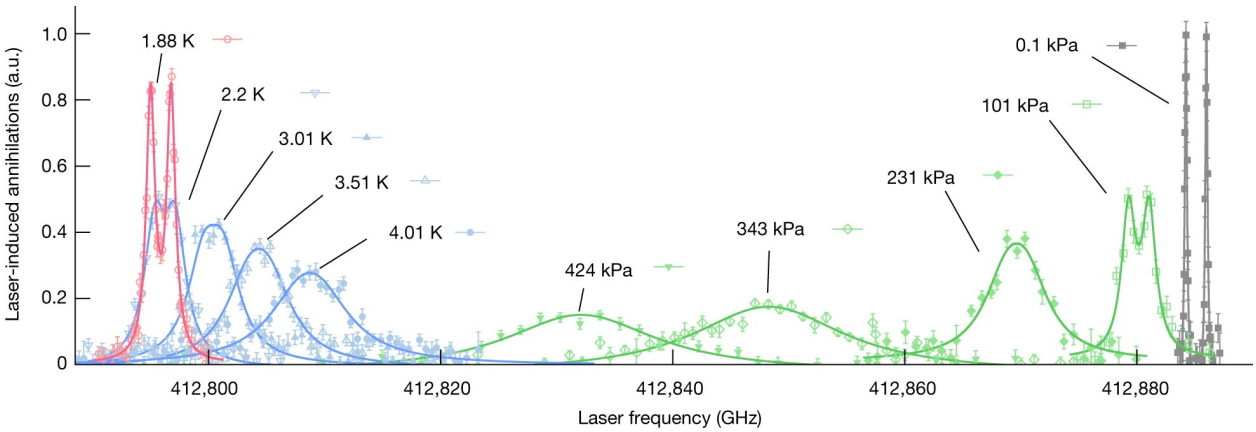

Figure 2 – Spectral lines measured in gaseous and supercritical helium (green data points) at pressures $p = 101$ kPa, 231 kPa, 343 kPa and 424 kPa, and temperature $T = 6.0$–6.4 K show progressively larger collisional shifts and broadenings relative to the data measured in gas of $p = 0.1$ kPa and $T \approx 1.6$ K (grey) with a linewidth $\Gamma_L = 0.19(3)$ GHz. The best fits of four overlapping Lorentzian functions are shown superimposed on each spectrum. Spectral lines observed in He-I (blue) of temperatures $T = 4.01$ K, 3.51 K, 3.01 K and 2.20 K became narrower as the liquid temperature was reduced. A rapid reduction of the linewidth below the He-II transition temperature revealed the hyperfine structure, with the sharpest spectral lines observed between $T = 1.78(2)$ K and 1.88(2) K (red). From Ref. [1].

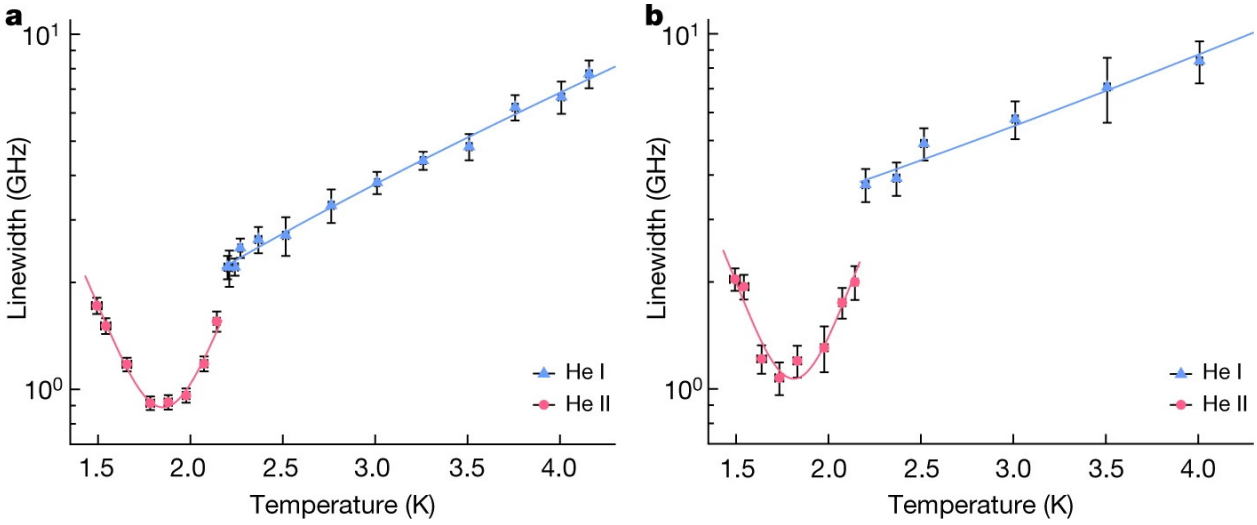

Figure 3 – The full-width-at-half-maximum Lorentzian linewidths of the transition $(n, \ell) = (37, 35) \rightarrow (38, 34)$ (a) and $(39, 35) \rightarrow (38, 34)$ (b). In He-I the temperature dependence of the linewidth was approximated by a single exponential (indicated by the blue curve), whereas in He-II a characteristic dependence with the smallest linewidths at temperatures between $T = 1.7$ K and 1.9 K was observed. From Ref. [1].

1.1 Anomalous spectral narrowing effect

Fig. 2A shows the spectra of the 726 nm resonance measured at six pressures of the gaseous and supercritical helium targets. The lineshapes contain contributions from the 21 MHz natural width, the laser linewidth, the hyperfine structure, power broadening effects, and the effects of the interactions with the surrounding helium combined with the motions of the atoms. The apparent full-width-at-half-maximum (FWHM) linewidths Γ_L were obtained by fitting the spectral profiles with four overlapping Lorentzian functions that were fixed to the relative positions of the calculated hyperfine intervals. The uncertainty was taken as the quadratic sum of the statistical uncertainty arising from the finite number of excited atoms and the systematic uncertainty. The latter includes contributions from the calibration and fluctuations of the target temperature and spurious shifts of 30–60 MHz in the laser frequency. The heating effect of the laser on the target was investigated using finite-element simulations.

As shown in Fig. 2, the resonance profile measured in a gas target of pressure $p = 0.1$ kPa and temperature $T \approx 1.6$ K [19] resolved the hyperfine structure as two distinct peaks. The best fit of four overlapping Lorentzian functions is indicated by the grey curve with a linewidth of $\Gamma_L \approx 0.19(3)$ GHz. When the pressure was increased by three orders of magnitude to $p = 101.4(1.4)$ kPa at $T = 6.4(4)$ K, collisions shifted the resonance centroid by $\Delta\nu = -4.94(5)$ GHz and broadened the linewidth to $\Gamma_L \approx 1.24(11)$ GHz as expected. With a further, twofold increase of the target pressure to $p = 231.1(1.4)$ kPa, the broadening became so great that the hyperfine structure could no longer be resolved (green curves). When the helium transitioned to supercritical phase of increasing pressure between $p = 343$ kPa and 555 kPa, the resonance further shifted from $\Delta\nu = -37$ GHz to -64 GHz and broadened to such a degree ($\Gamma_L = 15(2)$ GHz) that the $\overline{p}^4\mathrm{He}^+$ spectral line could no longer be resolved with a high signal-to-noise ratio.

In liquid helium, however, the 726 nm spectral lines became far narrower despite the higher atomic density of the target (Fig. 2). As the He-I target was cooled from $T = 4.16$ K to 2.20 K the

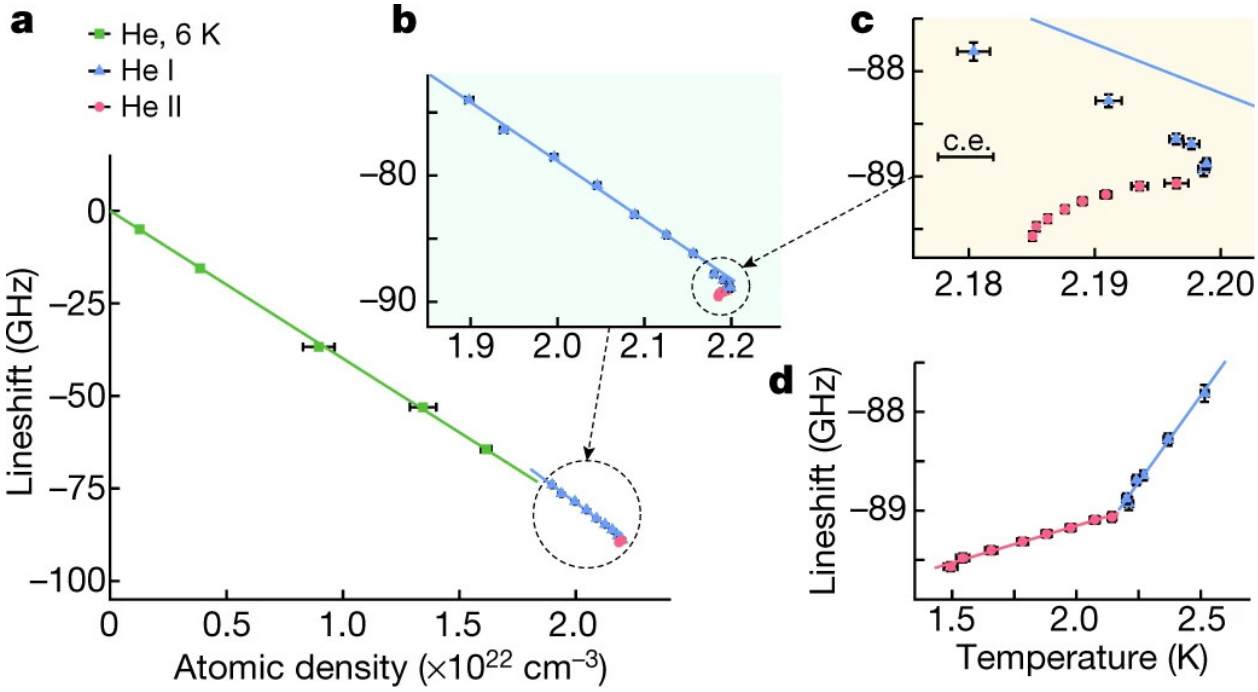

Figure 4 – Shifts in gaseous and supercritical helium (indicated by green squares), He-I (blue triangles) and He-II (red circles) targets relative to the zero-density transition frequency as a function of the atomic density (a). Magnified views of a, showing a deviation from a linear density dependence at target temperature $T < 2.5$ K (b,c). The results of the best fits of linear functions on the gaseous and supercritical helium (green line) and He-I (blue line) data at $T \geq 2.7$ K are shown superimposed. The size of the correlated uncertainty arising from the conversion of the liquid helium pressure and temperature into atomic density is indicated separately by the single error bar labelled as c.e. (d): The temperature dependence shows an abrupt change in the gradient $d\nu/dT$ at the He-II transition temperature $T_\lambda = 2.18$ K. From Ref. [1].

apparent spectral linewidth rapidly decreased from $\Gamma_L = 7.7(7)$ GHz to 2.21(17) GHz (see Fig. 3A). A similar reduction from $\Gamma_L = 8.4(1.1)$ GHz to 3.8(4) GHz was observed for the 597 nm resonance (see Fig. 3B). This temperature dependence of the spectral width Γ_L could be approximated by a single exponential (blue lines). An abrupt narrowing of the linewidth was observed below the He-II phase transition temperature $T_\lambda = 2.18$ K (see Fig. 3A) which unexpectedly revealed the hyperfine structure (Fig. 2) arising from the spin-spin interaction of the antiproton and electron. The highest resolution of ≈ 0.9 GHz for the 726 nm resonance was observed at a target temperature $T = 1.78 - 1.88$ K, while the 597 nm resonance narrowed to a linewidth $\Gamma_L = 1.07(11)$ GHz at $T = 1.73(2)$ K (Fig. 3B).

At a slightly lower target temperature $T = 1.49(3)$ K the spectral linewidths of the 726 nm and 597 nm resonances both increased by factor 2, to 1.72(9) GHz and 2.04(15) GHz, respectively. This resulted in the characteristic temperature dependencies shown in Figs. 3A–B which were fitted with parabolas. The spectral resolutions are an order of magnitude higher than the limits that would be expected according to the predictions of ab initio theoretical calculations [29, 30] for atoms of temperature $T \approx 5.4$ K using the impact approximation of binary collisions, which were based on pairwise potentials derived from the highly precise wavefunctions of $\bar{p}^4\mathrm{He}^+$. This implies that collective effects in the superfluid narrow the laser resonances below the limit expected from simple binary atomic collisions [20, 21].

1.2 Spectral shifts

In gaseous and supercritical helium targets, the centroids of the two resonances shifted linearly with target density relative to the zero-density frequencies (see Fig. 4A) with similar gradients $d\nu/d\rho \approx -(4.0-4.5)\times 10^{-21}$GHz·cm^3. This agrees with the results of previous experiments that were carried out in gas targets of much lower density, and with the predictions of the above binary collision calculations [29, 30]. Similar gradients were observed in He-I targets of temperatures between $T = 4.2$ K and 2.8 K. When cooled below 2.5 K, however, the gradients began to increase in a nonlinear way relative to density, before abruptly changing sign at the He-II transition temperature T_λ (details of Fig. 4A). The temperature dependence of the frequency shifts likewise appear to be roughly linear between $T = 2.2$ K and 2.55 K (Fig. 4B) with gradients $d\nu/dT = (3.5-3.9)$ GHz·K^{-1}, but in He-II the gradients abruptly decreased by a factor of 5–10. The onset of superfluidity thus affects both the shift and linewidth of the atomic resonances.

1.3 Discussion

Compared to the spectral lines at visible wavelengths of many other atoms and molecules embedded in He-II, the $\overline{p}\mathrm{He}^+$ resonances had symmetrical and sharp lines that abruptly became narrow below the superfluid transition temperature. This is believed to arise from the fact that the electron shell retains a radius $r_e \approx 40$ pm during the laser excitation which is an order of magnitude smaller than many other normal atoms. The perturbations to the surrounding He-II media as evidenced by the calculated $\overline{p}\mathrm{He}^+$-He pairwise potentials [20,21] are so small that the spectra are, we believe, sensitive to minute effects such as the abrupt changes in the number densities of elementary excitations that occur during the superfluid phase transition.

A strong excess in the flux of antiprotons or antideuterons of kinetic energy $E \leq 200$ MeV in cosmic rays is predicted to constitute an important indication of the dark matter that decay or annihilate in the halo of the Milky Way, or primordial black hole evaporation by Hawking radiation [31, 32] . The coolant liquid helium stored in some satellites or high-altitude balloons allow $E \leq 100$ MeV antiprotons come to rest and form $\overline{p}\mathrm{He}^+$.

2 Laser spectroscopy of antiprotonic helium atoms using ELENA

2.1 Beamline upgrades

The collaboration aims to carry out sub-Doppler two photon laser spectroscopy [16, 33] of atomic resonances which have not been detected yet but are predicted to have very small natural widths (≈ 0.3 MHz) using the ELENA [34, 35] beam, thereby improving the experimental precision by up to two orders of magnitude compared to before. This require many years of iterative work in terms of developing new metrological techniques and eliminating systematic uncertainties.

In 2021 the collaboration constructed and commissioned an electrostatic beamline that transported the 100 keV antiproton beam to the cryogenic helium target in which $\overline{p}\mathrm{He}^+$ atoms were formed. Three titanium ion pumps of pumping speed 500 liter/s, four turbomolecular pumps, and beam apertures and conductance limiters were used to isolate the helium gas target of pressure $P = 1.0$ mb and temperature $T = 1.5$ K from the ultrahigh vacuum in the other parts of the ELENA beamline of $P < 10^{-9}$ mb. This corresponds to a pressure differential of more than 9 orders of magnitude at room temperature. During the beamtime of 2021 it was found that the beam traversing the upstream quadrupole lenses had such small β-function values that even minor detunings of a few percent in the voltage settings caused significant changes in the focal positions. An alternative optical design involving larger β-functions caused some of the beam to be scrapped

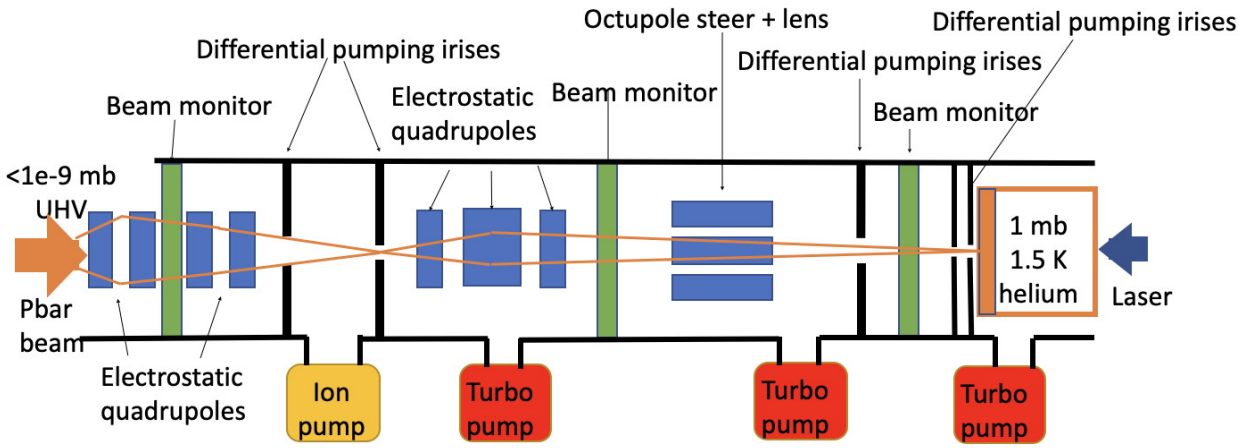

Figure 5 – Schematic drawing of beam transport line for laser spectroscopy of antiprotonic helium atoms with the upgrades installed 2022.

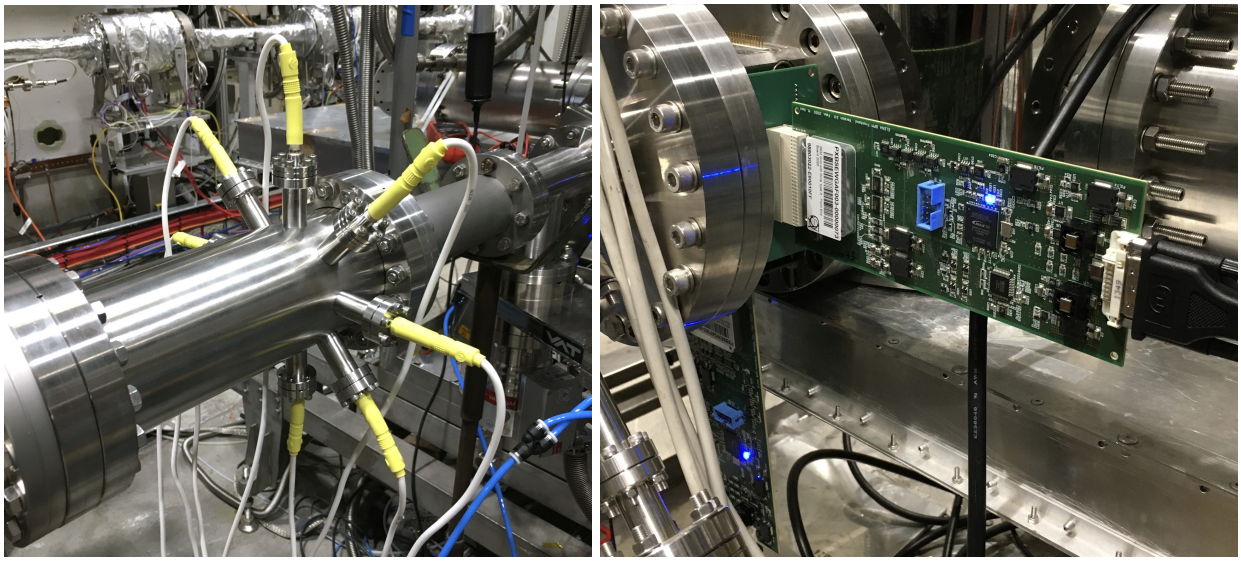

Figure 6 – Some of the new devices installed in 2022: octupole steerer and lens (left). ASIC-based readout electronics of the UHV compatible microwire secondary electron emission monitor of new design.

in the apertures and lost. Due to all these issues, the antiproton beam could not be precisely focused into the experimental target to observe the laser resonance of antiprotonic helium during the initial commissioning run of 2021.

During 2022, to remedy these problems electrostatic octupole deflectors (see Fig. 6, left) and lenses of inner diameter $d = 80$ mm, and beam apertures were installed. A new beam profile monitor based on secondary electron emission [36] which were read out by an application-specific integrated circuit (ASIC) and field programmable gate array (FPGA), (see Fig. 6, right) was constructed, commissioned, and installed. The newly upgraded beamline (see Fig. 5) was then recommissioned.

Fig. 7(a) shows the horizontal and vertical dispersions σ of the beam measured along the beamline using the four secondary electron emission monitors for various voltages applied to two

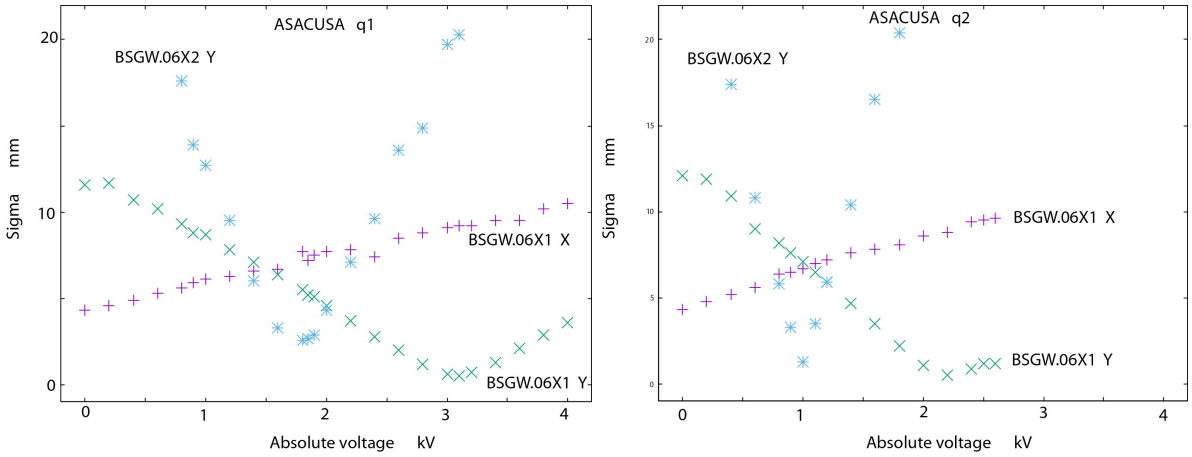

Figure 7 – The dispersions of the antiproton beam in σ measured by the four beam profile monitors as a function of the voltage setting on two electrostatic quadrupoles q1 and q2. The effective gradient of the quadrupole lenses determined from these measurements deviated from some of the values used to design the beamlines by between 10% and 30%. This is believed to be due to the effects of fringing fields and by the complex design of the beamline.

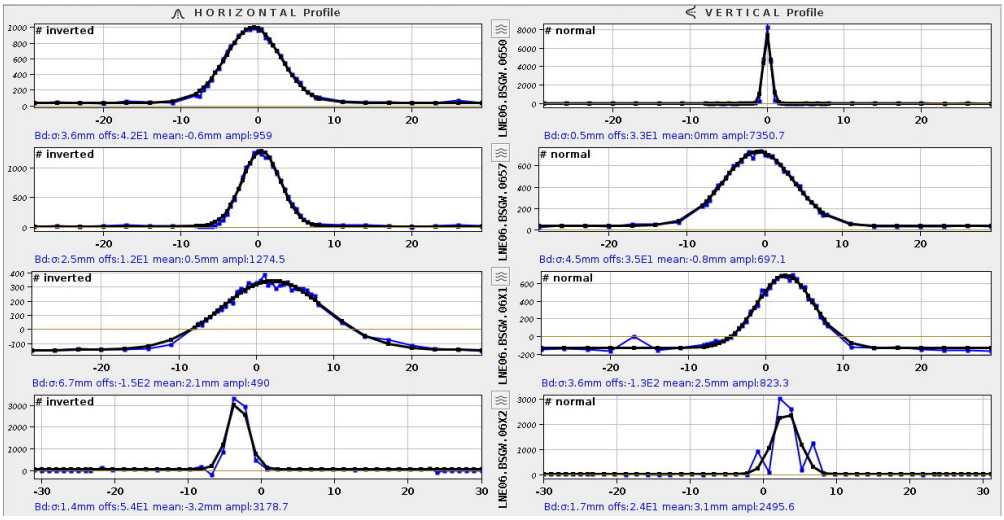

Figure 8 – The horizontal and vertical spatial profiles of the antiproton beam along the beamline. As a result of the 2022 upgrades, the full horizontal and vertical beam diameters at the position of the experimental target was reduced to 7 mm and 9 mm, respectively.

quadrupole lens elements. The effective gradient of the quadrupole lenses determined from these measurements deviated from some of the values used to design the beamlines by between 10% and 30%. This is believed to be due to the effects of fringing fields and by the complex design of the beamline. After several such optimizations, we managed to tune the antiprotons so that they were first focused to $\sigma \leq 1$ mm and allowed to pass through an racetrack-shaped aperture of 8 mm $\times$ 20 mm. The beam expanded over a distance of 2.5 m and traversed two apertures before being refocused by an electrostatic quadrupole doublet and then by an octupole steerer and lens. A beam of horizontal and vertical dimensions of 7 mm and 9 mm arrived at the target. This is up to 40%

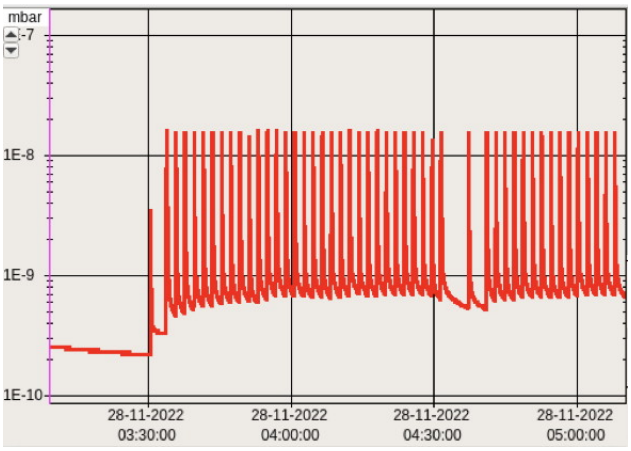

Figure 9 – Time evolution of the vacuum level in the ELENA transfer beamline due to helium leaking from the cryogenic experimental gas target over a 2 hour period. A gate valve was used to isolate the experimental target from ELENA. The valve was opened for a few seconds to allow the antiprotons to arrive at the target. The pressure increased in synchronization with the opening of the valve. This allowed laser spectroscopy to be carried out. In 2023 we plan to improve this vacuum pressure by nearly two orders of magnitude.

larger than the results of simulations used to design the beamline. The reason for this is unknown.

2.2 Observation of laser resonance

We then carefully tuned the antiproton beam so that it traversed a 6 mm diameter window made of polymide and entered the cryogenic target. The focus was quite sensitive to small $< 0.2\%$ changes of the voltages applied to the electrodes, and so precision high-voltage power supplies were used. This resulted in the formation of metastable $\overline{p}\mathrm{He}^+$ atoms.

An injection-seeded titanium sapphire laser of wavelength $\lambda = 726$ nm and pulse energy 10 mJ was fired into the experimental target. This induced the transition $(n, \ell) = (37, 35) \rightarrow (38, 34)$. A laser resonance signal was detected with an intensity of 1/2 compared to the values measured previously using the radiofrequency quadrupole decelerator (RFQD). The hyperfine structure arising from the spin-spin interaction between the antiproton and electron was resolved. We have thus successfully demonstrated laser spectroscopy of antiprotonic helium atoms using ELENA.

2.3 Helium accumulation in ELENA

Further improvements and optimizations in the laser resonance signal were hampered by the small amount of helium gas permeating through the polymer beam window of the cryogenic target. This gas entered the beamline and traversed the beam apertures. As the ELENA vacuum system is not designed to pump helium gas, the helium eventually accumulated in ELENA and caused up a 20% reduction in the antiproton beam intensity.

We temporarily solved this problem by adding turbo molecular pumps and apertures in the beamline. A gate valve was used to separate the cryogenic target from the experimental beamline leading to ELENA during the 120 s intervals between antiproton arrivals. The valve was opened for a few seconds in synchronization with the extraction of antiprotons from ELENA to allow them to reach the target. Pressure spikes were detected (see Fig. 9) whenever the valve was opened, but the loss of circulating antiprotons in ELENA was prevented. This allowed laser spectroscopy

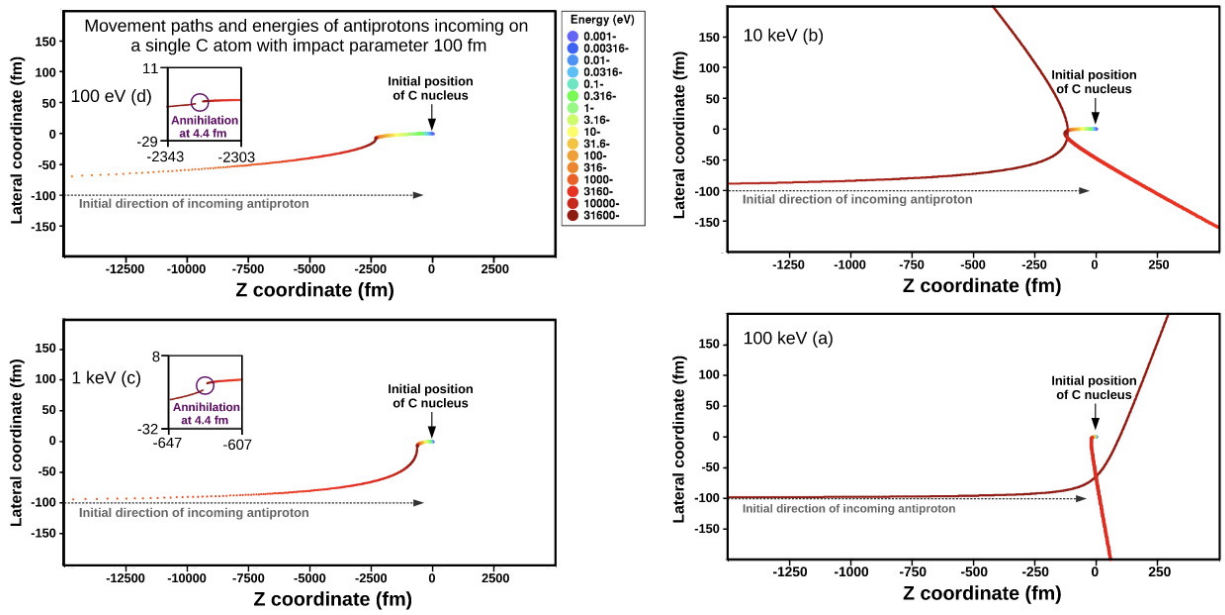

Figure 10 – Trajectory of an antiproton with an impact parameter b = 100 fm and incident energy of 100 keV (a), 10 keV (b), 1 keV (c), and 100 eV (d) scattering off a single carbon atom positioned at the origin calculated by MD-RIA. Note the different horizontal and vertical scales. The gradients indicate the kinetic energies of the antiproton and C atom in logarithmic scale. Annihilations occur when the antiproton comes within 4.4 fm of the C atom. From Ref. [37]

measurements to be continued, but the amount of helium gas that we could safely introduce into the target was thus limited.

For 2023 we intend to extend the beamline by 4 m and install further apertures and a quadrupole triplet lens. This is expected to reduce the helium gas entering ELENA by more than two orders of magnitude.

3 Reorientation of the collaboration

The laser spectroscopy of antiprotonic helium has been funded and carried out primarily by PhD students and researchers with non-permanent positions that were affiliated with, e.g., Max-Planck Institute of Quantum Optics on time-limited contracts and competitive research funding. As the experiment unfolded over the last two decades and especially in the last 6 years it has become vitally important for the main contributors to find permanent academic positions to ensure the continuation of the experiment. Since 2017 time was increasingly diverted to accumulating university teaching experience and to job search efforts. The most time was spent on these efforts away from CERN in 2022. These generation-changing efforts will be largely completed during 2023, so that the experiment can be continued for the foreseeable future. The main contributing institutions during 2023 will now include Johannes Gutenberg University Mainz and Imperial College London.

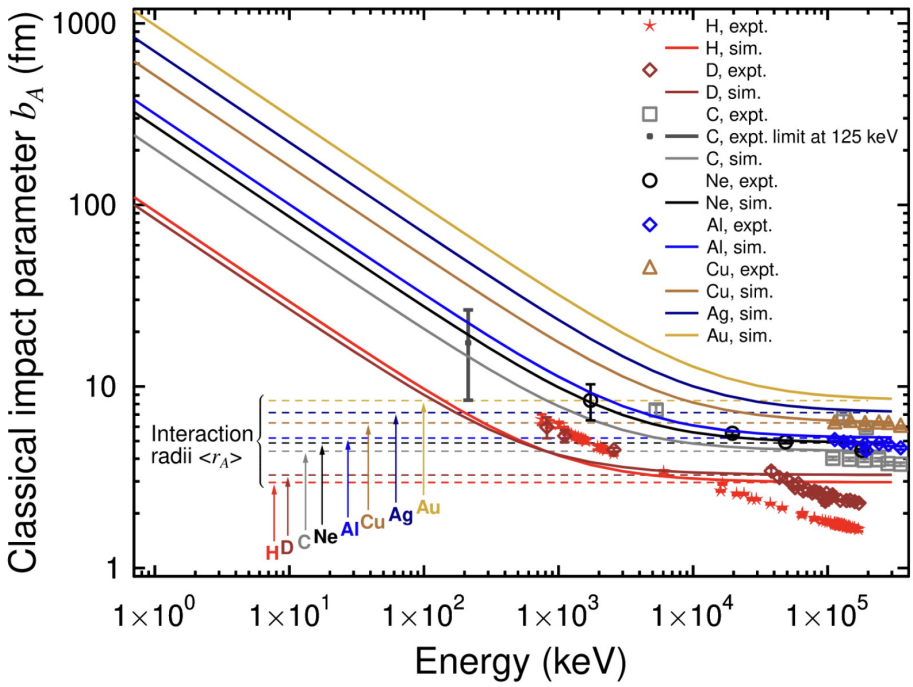

Figure 11 – Minimum impact parameter b_A of an antiproton colliding with a H, D, C, Ne, Al, Cu, Ag, or Au atom that leads to in-flight annihilation as a function of the incident energy calculated using MD-RIA. The simulations utilized the average interaction radii according to Eq. (4) of Ref. [38] shown in the figure for each target. The experimental values of H, D, C, Ne, Al, and Cu targets that were obtained from the measured annihilation cross sections. The vertical line with error bars for C at 125 keV represents the experimental limit of Ref. [39]. The curves are arranged in the same sequence as in the indicated labels. From Ref. [37].

4 Improved MD-RIA calculations of antiproton transmission through polymer foils

During 2023, a theoretical paper in collaboration with the Helsinki group [37] was published. The transmission of antiprotons through the polymer and metallic foils [40–47] were simulated using the molecular dynamics approach in the recoil interaction approximation (MD-RIA) [48, 49]. This multi-body method numerically solves the equations of motion for every simultaneous collision that occurs between the antiproton and multiple atoms in the precise antiproton-atom chemical potential, as the trajectory of the antiproton is tracked within the foil. The nuclear stopping and elastic scattering [39, 50, 51] which are predicted by some theories to become dominant at keV energies just prior to the emission of the antiprotons from the foil are included.

In some of the MD-RIA simulations a more complex model that takes both the in-flight annihilations of antiprotons at keV-energies and the capture of sub-1 keV energy antiprotons into account was used. Annihilation occurs when the antiproton comes within the effective interaction radius $r_{\rm A}$ of the nucleus which is taken to be independent of the incident energy. This black disk model is believed to be valid for massive target nuclei with diameters that are sufficiently large compared to the wavelength of the antiproton [38, 52]. We used the average interaction radius,

$$\langle r_{\rm A} \rangle = 1.840 + 1.120(A)^{1/3} \text{ fm}, \tag{1}$$

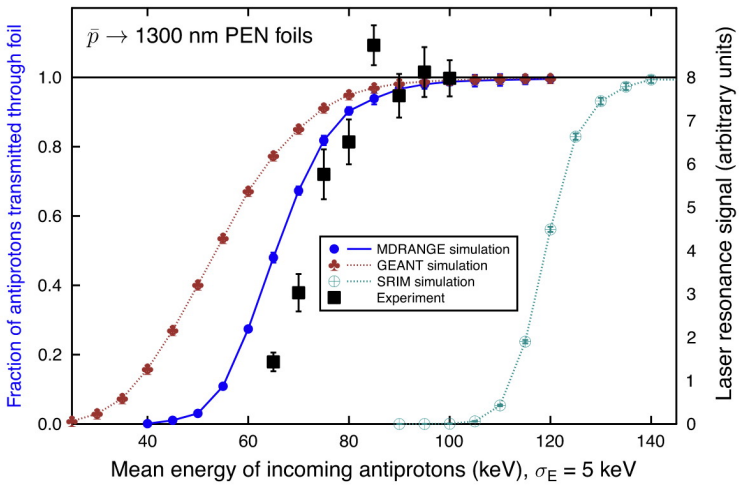

Figure 12 – Relative intensities (filled squares) of antiprotons transmitted through a 1300-nm-thick PEN foil measured by laser spectroscopy of antiprotonic helium as a function of the incident beam energy. The results of MD-RIA simulations with (filled circles) and without (open triangles) the nuclear scattering and stopping Sn. The results of the GEANT4 code, and the proton result of SRIM2013 are shown superimposed. From Ref. [37].

that was derived from the unified optical potential model of Ref. [38]. Eq. 1 was obtained by folding the optical potential of the antiproton-proton system that was obtained from experiments carried out at $E_k \approx 750$ keV, with the matter density distributions of the nuclei. Comparisons with the results of x-ray spectroscopy experiments of antiprotonic atoms with mass number $A > 10$ have shown that the model reproduces the shifts and widths of the atomic energy levels that arise due to the strong interaction [38]. These spectroscopy measurements effectively study the antiproton-nuclei scattering at nearly zero energy.

The simulated trajectories of antiprotons with impact parameter $b = 100$ fm and incident energies $E_k = 100$ keV and 10 keV that scatter off C atoms are shown in Figs. 10(a) and (b), respectively. At lower energies $E_k = 1$ keV (Fig. 10(c)) and 100 eV (Fig. 10(d)), the more pronounced curvature of the trajectories allow the antiprotons to approach the nuclei within the $\langle r_{\rm A} \rangle = 4.4$ fm distance implied by Eq. 1 and annihilate.

Fig. 11 shows the values of the maximum impact parameter $b_{\rm A}$ that leads to annihilation in H, D, C, Ne, Al, Cu, Ag, and Au nuclei that were determined in this way. Antiprotons of high energy ($E_k \gtrsim 5$ MeV) approach the nuclei along straight trajectories so that the impact parameter $b_{\rm A}$ is roughly equal to $\langle r_{\rm A} \rangle$. At lower energies, the focusing effect of the Coulomb force causes $b_{\rm A}$ to rapidly increase. The results were compared with the experimental cross section $\sigma_{\rm A}$ of antiproton annihilations which were taken to relate to the impact parameter as $\sigma_{\rm A} = \pi b_A^2$. The lack of experimental data at energies below a few MeV makes this comparison difficult, but the simulation and experimental results are consistent for C, Ne, Al, and Cu targets within the experimental uncertainties. Deviations are seen in H and D for which the semiclassical parameterization of Eq. 1 is not expected to be a good approximation. Indeed, partial-wave decomposition analysis [53, 54] have shown that the cross sections for these light nuclei at low energies are dominated by the contributions of the s- and p-wave components of the approaching antiproton. The fraction of $E_k = 1$–100 keV antiprotons that undergo in-flight annihilation is relatively small (see below), as the corresponding b_A values of approximately 10–1000 fm are 2–4 orders of magnitude smaller than

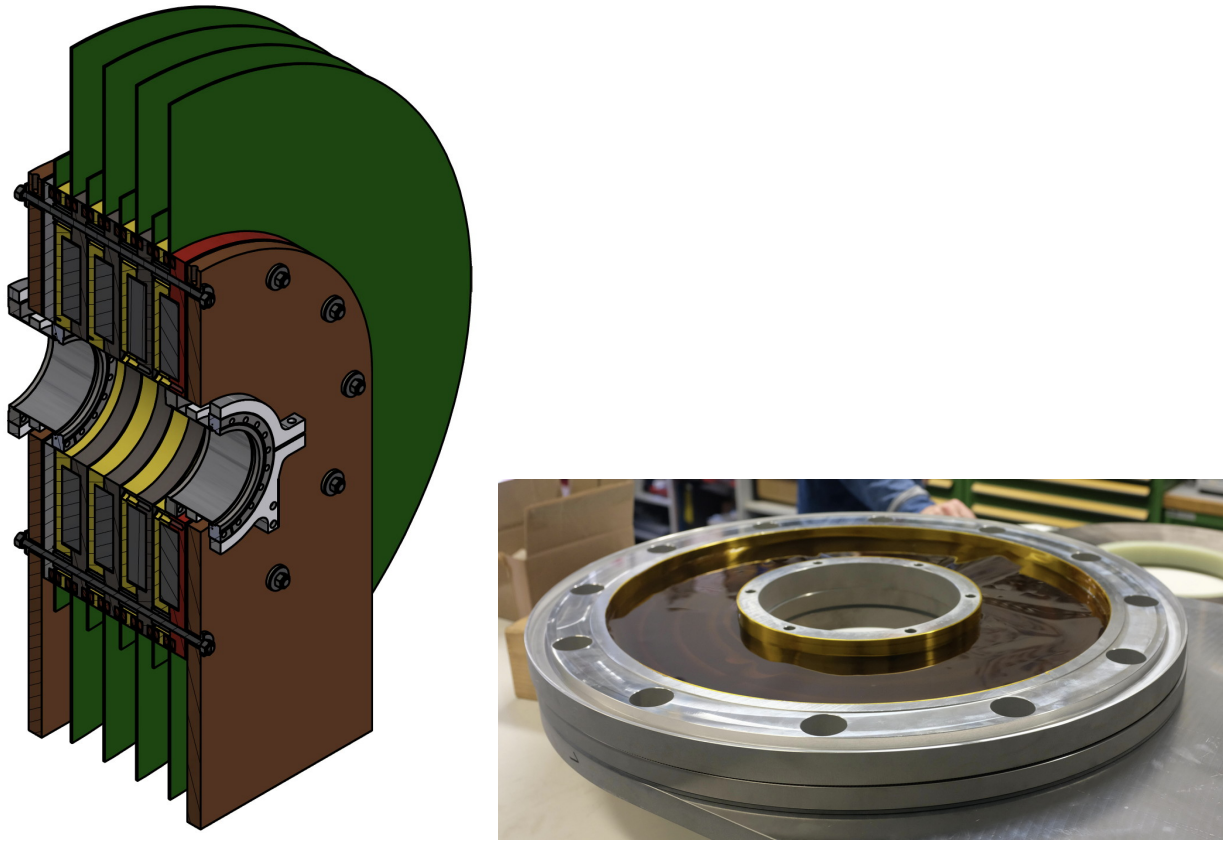

Figure 13 – Induction decelerator now being machined in Mainz (left). One of the deceleration cells (right).

the interatomic distances of ≈ 100 pm.

As shown in last year's report, Fig. 12 gives the relative intensities of antiprotons that traversed the cryogenic $t_r = 1300$ nm thick polymer window and came to rest in the helium target. The intensity of the laser spectroscopic signal [16, 19] was measured as a function of the incident energy $E = 63$–98 keV of the antiproton beam (filled squares with error bars). A good agreement between the experimental and MD-RIA simulation results (blue solid curve) is seen within the systematic uncertainties of the foil thickness and uniformity.

5 Induction decelerator

ASACUSA continued the development of the induction decelerator (see Fig. 13) which would allow the antiproton beam to be slowed down to much lower energies < 40 keV in a highly reproducible way with minimal energy spread and radiated radiofrequency noise. The detrimental effects of decelerating from 100 keV using only a foil can then be reduced and a sample of $\bar{p}\mathrm{He}^+$ atoms of much greater density and small geometric size produced. With the move of the antiprotonic helium group to Mainz and with the securing of funding, we have launched the production of ten deceleration cells for the device. The device will be assembled in the superconducting radiofrequency cavity assembly hall in the Helmholtz Institute Mainz.

6 Preparations for the 2023 beamtime

In 2023, we plan to extend the beamline by 4 meters and install additional electrostatic quadrupole lenses, apertures, and turbo pumps to reduce the helium gas load into ELENA by two orders of magnitude. We will then reoptimize the laser spectroscopic signal of antiprotonic helium, and search for the four most intense two-photon transitions [14,33] $(n,\ell) \rightarrow (n-2,\ell-2)$ of the $\overline{p}^3\mathrm{He}^+$ and $\overline{p}^4\mathrm{He}^+$ isotopes.

In terms of the ultrastable optical fiber signal. Discussions between ALPHA, ASACUSA, SWITCH, METAS, and the universities of Basel and Geneva continue in the context of the Swiss Quantum Communication Infrastructure (Swiss-QCI) proposal to construct among other things a ring topology network that connects METAS with Neuchatel, Geneva, CERN, CSEM, EPFL, and other commercial users. The French NREN RENATER and the Polish research institutes plan to also send an ultrastable fiber signal from Observatorie de Paris and Poznan to CERN.

Part II
Antihydrogen

In the summer of 2022, a paper describing the work to produce cold plasma in the Cusp trap detailed in previous SPSC reports [55] is published in the AIP Physics of Plasmas journal (see reference [56]). In this work we demonstrated that it was now possible to produce cold dense plasma in the Cusp trap with a port open to a room temperature pipe with a large solid angle for antihydrogen atoms to exit the production region. In principle, we were now ready to test mixing with cold plasma, however one large and important task remained from LS2 which was the upgrade of our positron system. As is detailed below, this was no simple task and resulted in delays to our program in 2022.

Although it was not possible to progress as much as we hoped in terms of antihydrogen production this year, a great deal was achieved. The experiment has undergone a complete upgrade of its control system. All traps are controlled by real-time targets and interfaced via the same software suite. This greatly simplifies operation and increases the pool of people who can operate all three traps. The MUSASHI antiproton trap cycle time has been reduced to of the order of 110 s, the same as 1 ELENA bunch. This will greatly improve efficiency for mixing experiments and eventually beam production compared to the 3-5 cycles used previously [57]. The old positron trap which used 1000 l of LHe a week has been replaced with a new model with a water cooled magnet. Positrons have been trapped and caught in the accumulator, then bunches transferred from the accumulator to the cusp (albeit with a low number of positrons). The microwave cavity and sextupole magnet were brought out of storage and moved to the ASACUSA area where they were recommissioned ready for use. The antihydrogen detector upgrade was finished and returned from Vienna with a much higher readout speed which is essential for shorter mixing cycles and the greater antihydrogen yield expected from the reduced plasma temperature. The refurbished scintillating bar detectors were installed and tested for the first time since they were upgraded from PMT readout to SiPM in Brescia.

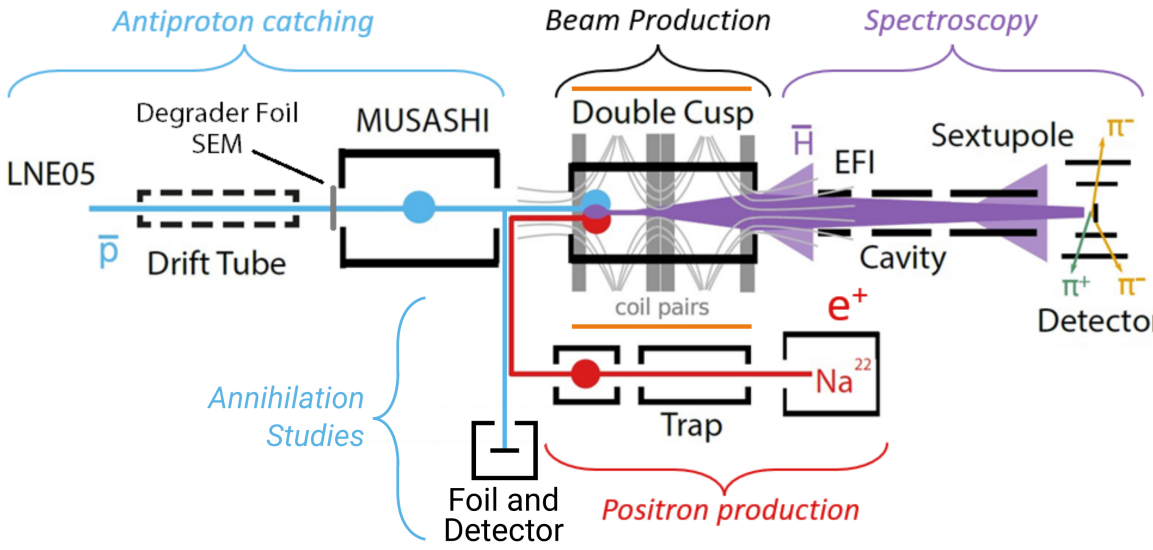

Figure 14 – Schematic diagram of the ASACUSA-Cusp experiment. Position of the scintilating bar detectors shown in orange eitherside of the Cusp trap.

Details of all our work in 2022 and a plan for 2023 are given below. To aid the reader, a schematic diagram of the ASACUSA-Cusp experiment is shown in fig. 14.

7 Antiprotons

7.1 Antiproton trapping in MUSASHI

The LNE05 beam transport line used by the the ASACUSA Cusp experiment was completed in 2022. The missing Secondary Electron Monitors (SEM) were installed, and the line was re-aligned by the CERN surveyor. Working with the CERN specialist we improved the beam focusing for the experiment and corrected some optics mismatches, resulting in a more stable beam entering into to the MUSASHI trap. However, measurements still show a misalignment for the fine focusing on the degrader foil/SEM located at the entrance of the MUSASHI trap [58] (cf. Fig. 14), e.g. the Y profile shown in Fig. 15 does not match the X profile. As a result, the incoming beam has an ellipse-like shape although calculations predicts a round profile. Furthermore, some fraction of the incoming $\overline{\mathrm{p}}$ beams were lost at the entrance of the drift-tube electrode (see fig 14), indicating a larger radial size than expected. The efforts to tune the beam with the specialist will continue into the year 2023.

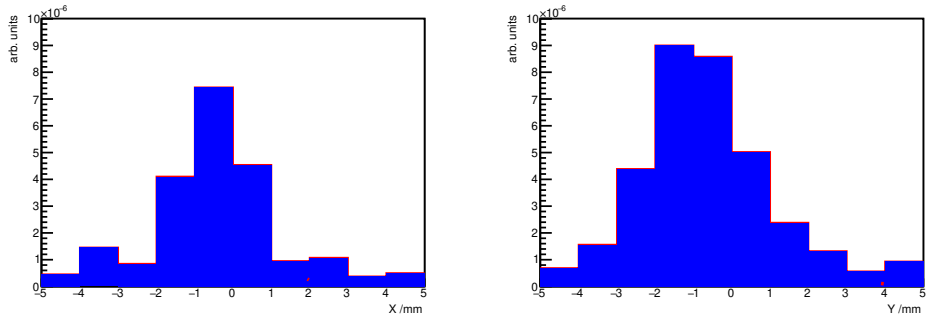

Figure 15 – A beam profile observed with the foil detector, which shows $\sigma_x = 0.9\,\mathrm{mm}$ and $\sigma_y = 1.6\,\mathrm{mm}$.

Though the steering and focusing of the injected $\overline{\mathrm{p}}$ beam might not be the optimised, the drift tube energy adjuster and the MUSASHI trap have worked stably without any critical problems. The MUSASHI trap successfully cooled at least 1.6×10^6 $\overline{\mathrm{p}}$ among those captured for one ELENA spill. Figure 16 shows the typical counts from antiproton annihilation during one cycle of capture, cool, and release. The trapping well was slowly ramped up such that antiprotons were guided to the degrader foil where they annihilated, and were counted using one set of 2 m-long scintillator bars.

The production cycle of the ultraslow antiproton beam was shortened for efficient use of ELENA cycle and hence, synthesis of $\overline{\mathrm{H}}$ atoms. After electron cooling, the antiproton cloud was radially compressed with an electron plasma where the ratio of antiprotons to electrons was 1:100 using a strong rotating electric field after which $> 90\%$ of electrons were removed. Antiprotons were extracted together with the remaining electrons after an additional radial compression. All these process fit within one AD-ELENA cycle, 110.4 s. Antiprotons at larger radii (from the larger beam spot discussed above) were not well cooled with the reduced time, this fraction was around 10–20% and difficult to compress. The extracted antiproton beam at 100 eV had a 2 µs bunch length. The capture timing at the Cusp trap was adjusted for the antiproton beam transit time. As a result, the remaining electrons extracted with $\overline{\mathrm{p}}$s did not greatly affect the antiproton transportation. The

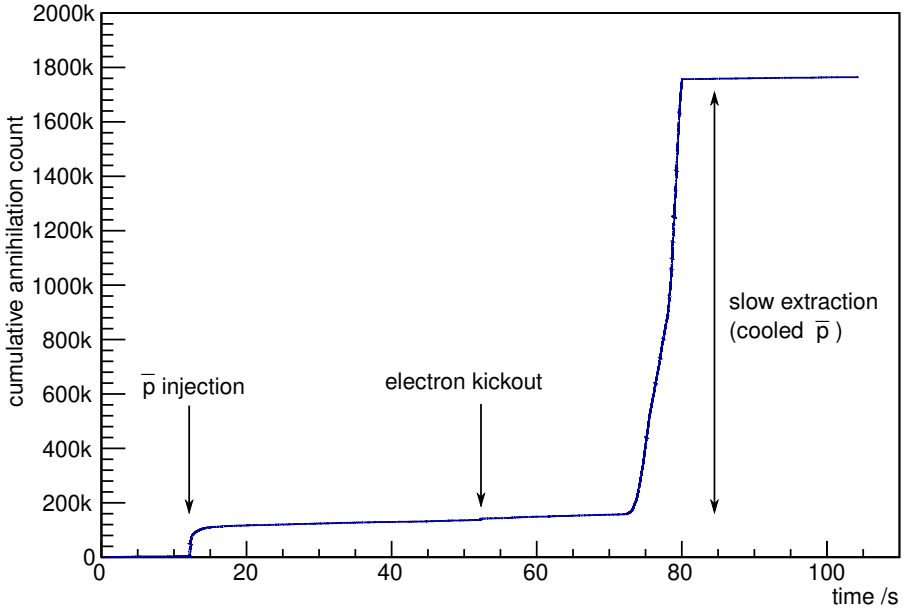

Figure 16 – Counts of $\overline{\mathrm{p}}$ annihilation during one cycle of capture, cool, and release from Musashi trap.

developed time-optimised operation scheme was also applied to a slow extraction beam operation for some tests with the $\overline{\mathrm{H}}$ detector (Sec. 9.2).

Although the number of trapped antiprotons was improved in 2022, another factor limiting the trapping efficiency is the energy spread of the $\overline{\mathrm{p}}$ beam emitted from the degrader foil. Measurements indicate a lower incoming energy from ELENA in combination with a thinner foil would help to reduce the degraded beam energy spread. Reducing the ELENA energy is not a solution at present, thus, we have started to modify the existing foil detector, where the silver plating will be replaced by aluminium plating to reduce the nuclear scattering. This is expected to produce a degraded beam which has a lower divergence and narrower energy spread and thus is easier to trap.

7.2 Antiproton trapping in the Cusp

Antiprotons were transferred from MUSASHI to the Cusp trap focused by an electrostatic lens and guided by several magnetic coils with a transport energy of 100 eV. A preloaded electron plasma cooled antiprotons after catching in in the Cusp trap. A rotating wall recompressed the antiproton cloud with the cooling electron plasma. The Cusp electrode stack has two sets of segmented electrodes for manipulation of positron and antiproton/electron plasmas.

The Cusp plasma detector (MCPPS) consists of a single microchannel plate (MCP) and a fast phosphor screen (p46), allowing particle detection with sub-μs timing resolution. The time dependent light signal from the PS is recorded by a silicon photomultiplier (SiPM). This device easily achieves single-particle sensitivity for antiprotons. It is possible to release the antiprotons from the Cusp slowly enough (about 40 ms) such that the detector does not saturate. The total number of antiprotons is given by the time integral of the total SiPM signal, minus background, divided by the integral of a single antiproton signal.

By slowly dumping antiprotons, we counted the cooled antiprotons extracted from the Cusp trap to the MCP. In addition, seven scintillator bars surrounding the Cusp cold bore count antiprotons

annihilated in the electrode stack during radial compression or potential manipulations. Combining those counts, we estimated that the Cusp trap caught 4×10^5 $\overline{\mathrm{p}}$s for every MUSASHI cycle. Among them, $> 2 \times 10^5$ $\overline{\mathrm{p}}$s were compressed in the Cusp trap, which is usable for antihydrogen production.

The antiprotons were held in the 6 K trapping region of the Cusp for up to 300 s and then extracted to the MCPPS. The number of detected antiprotons varied randomly as a function of holding time, with a relative standard deviation of 13%. This was the first measurement of the antiproton lifetime in a trap with graphite-coated electrodes. The measurement establishes the usefulness of colloidal graphite for antiproton traps and also implies that the pressure in the Cusp trap was not higher than 10^{-12} mbar. Since the fluctuations showed no correlation with holding time, they were probably due to variation in initial conditions. For example, the integrated beam intensity on the downstream side of the foil detector (at the entrance to the antiproton trap) also varied by 13% during this experiment.

The MCPPS detector provides a 2D profile of extracted plasmas. Figure 17(a) shows an image of a compressed antiproton cloud with electrons. A magnetic field coil placed perpendicular to the beam axis produces a field that deflected light particles. Thus, electrons were moved away from the active detection area, which produced images of the pure antiproton cloud. Another scheme to obtain a compressed antiproton cloud was studied, in which electrons were removed from the trapping well prior to radial compression. The trials indicate compression of the antiproton cloud, as shown in Fig 17(b), though some fraction was lost during the operation.

The temperature of plasmas after electron cooling and manipulation was investigated using the method developed for electron plasma [56]. The preliminary results show 120 K for electron plasma with antiprotons. When the transverse coil deflected electrons to detect only antiprotons on the MCP, the temperature measured was 6000 K. These measurements indicate that the electron-cooled antiprotons could be mixed with a large number of positrons to produce colder $\overline{\mathrm{H}}$ atoms.

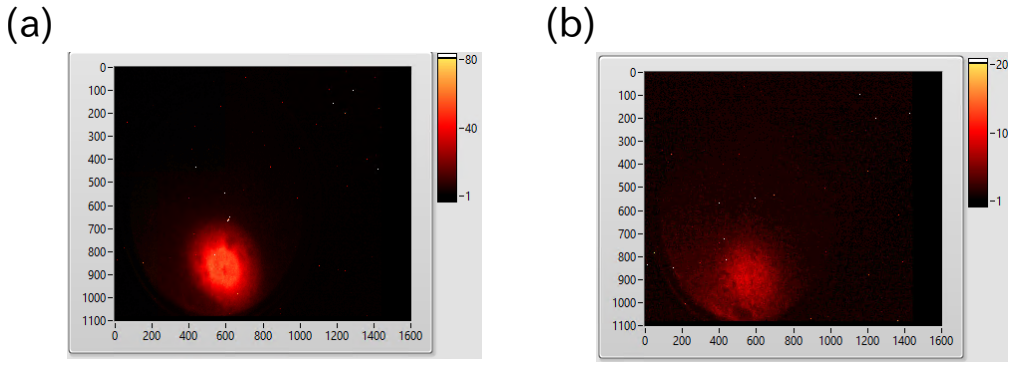

Figure 17 – (a) Compressed combined $\overline{\mathrm{p}}$ and electron plasma. (b) Compressed $\overline{\mathrm{p}}$ cloud after removing electrons using the transverse coil.

7.3 Scintillating bar detector

The scintillating bar detector consists in 8 $\sim$1 m^2 panels, each made of 60 scintillating bars, placed beside the cusp trap (cf. Fig. 14) in a XY configuration in order to allow the detection of the charged pions emitted by $\overline{\mathrm{p}}$ annihilations inside the trap. The annihilation time is measured and the vertex position is reconstructed with an expected resolution of a few cm in the longitudinal coordinate.

The detector light readout system was upgraded before the beam time: the Multi-Anode Photomultipliers have been replaced by SiPMs and the internal mechanism as well as the front-end

electronics boards have been refurbished or redesigned to cope with the new sensors. More details about the upgrade and the test with cosmic rays are reported in [59].

In Fig. 18 a plot of the annihilation vertex z position from a sample run is shown: in this case the antiprotons are initially confined for a relatively short time around a known electrode position (0 mm represents the cusp trap centre) and then they are slowly released. As shown in Fig. 18 the spatial resolution agrees with expectations.

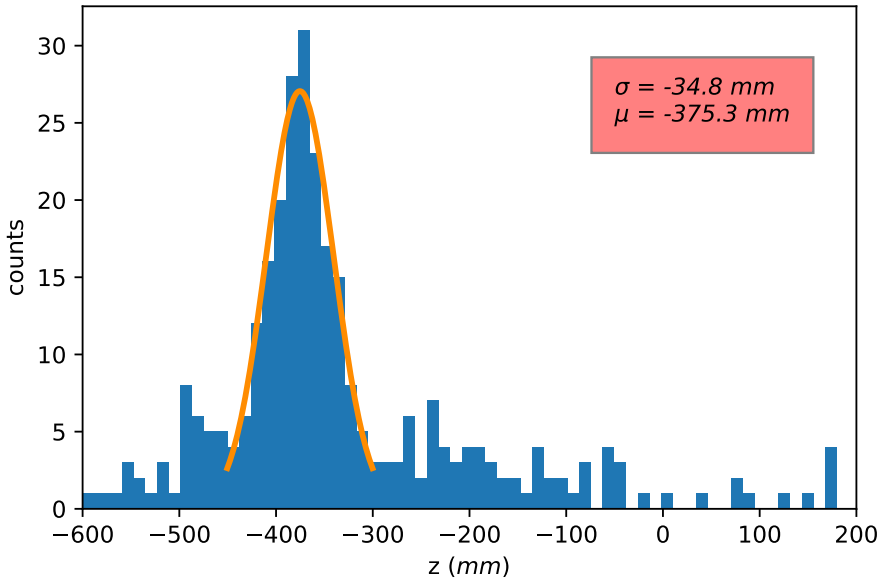

Figure 18 – Longitudinal coordinate of the antiproton annihilation vertex as reconstructed by the scintillating bar detector. In this run the antiprotons were held in a three-electrode well with spatial extent $-390 < z < -320$ mm. The antiprotons annihilated on residual gas in the room temperature trap.

Data taken in 2022 has been used to calibrate the detector, establish the best settings to operate in the current geometry and improve the integration level of the detector DAQ to allow a better coordination with the main cusp DAQ system, a goal that had not yet been achieved.

8 Positrons

Since the submission of our new proposal in 2019 [60], we have planned to replace our existing rare gas moderator (RGM) and positron trap which was housed in the cold bore of a 5 T superconducting magnet, with a commercially available First Point Scientific (FPS) model. This existing apparatus was characterised and used at Aarhus University for many years so its performance was well known. The change also necessitated the development of an accumulation stage before the Cusp trap. This is due to the much lower lifetimes (because of higher gas pressures) in the new trap. This provided the opportunity to develop an accumulation stage which could transfer all the positrons for a mixing cycle in a single shot, thus reducing the gas contamination transferred to the Cusp before mixing which results in loss of antiprotons. Removing the superconducting magnet also removed the need for deliveries of 1000 l of liquid He per week to use our positron system.

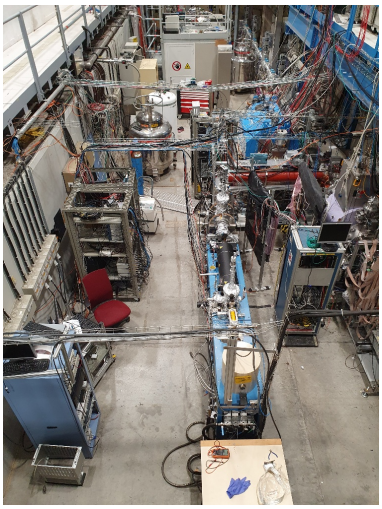

Figure 19 – Photograph of the new First Point Scientific rare gas moderator and trap.

The apparatus was transported from Aarhus in late 2019 and was unfortunately heavily damaged during this shipping and unloading in our lab at Bat. 15. The transported equipment consisted of 2 parts, the RGM, and the trap. It was planned to bring this equipment online in 2020/21 during LS2 in bat. 15 before transporting it to the AD hall. Unfortunately, this was not possible during the pandemic working conditions at CERN and elsewhere. Hence, the system had to be built and tested online during the 2022 beam time.

In 2021 a new 1850 MBq ^{22}Na source was ordered from iThemba laboratories, we were expecting to take delivery of this source in July of 2022. Due to delays at iThemba caused by Covid, the source still has not been produced at the time of writing this report. The new source is expected to be delivered in early 2023.

8.1 Positron trap

The trap and RGM were moved to the AD hall in January of 2022, at this time we discovered that a major maintenance cycle on all cold heads and compressors was required as these were many thousands of working hours overdue. The 4.2 K cold head used to grow the Ne moderator in front of the source had to be returned to ARS in the United States and was not returned until June. As we would not be able to work with positrons in that time an electron gun was added. As mentioned above, due to poor handling during shipping, almost every vacuum chamber on the RGM had damage resulting in leaks which had to be repaired by the CERN workshop. Some of the original pumps were replaced with newer models again due to shipping damage and their age.

The trap fared better, with only minor problems in the vacuum system, which could be repaired by ourselves and with one electrode dislodged. However, after some months of operation the main cryopump malfunctioned. We were unable to purchase replacement parts via CERN due to difficulties with advance payments to a small company in the US, hence it was replaced with a 700 l/s turbo molecular pump which compared to a 21,000 l/s cryogenic pump is a significant downgrade.

During this time, a weak (113 MBq) sodium-22 source was transported from Denmark to CERN. The old RGM used a different mounting system for the source, but has approximately the same activity as the source from Denmark, so it was decided to use the latter one. It is simpler and safer to use a source installed in the correct holder and stored inside the appropriate transfer device than

to move a source into a new holder. This was installed very shortly after the source cold head was returned so positron experiments could finally begin at the middle of July. It was quickly possible to grow moderators and then begin trapping shortly after. During these initial tests, the moderator decayed by approximately 1.5 % per hour which was higher than expected, showing there was some contamination around the source area. The lifetime of the positrons was measured for different gas pressures and found to be around 1 s, and initial trapping experiments were able to accumulate a few thousand positrons.

We suffered yet more problems due to the transport shortly after these first results, when the solenoid magnet for transporting the low energy positron beam from the source region to the trap began shorting to ground. To repair this, the source had to be removed and part of the magnet cut back to allow rewinding of corroded magnet wire. This process caused significant delays so no positron experiments were possible between the end of August and the middle of October when the source was finally reinstalled.

In the final 6 weeks of the shortened beam time, all efforts concentrated on increasing the number of trapped positrons. Using a calibrated gamma-ray detector, we were able to determine that approximately 140 k positrons per second were entering the trap. For the 130 MBq source, this yields a moderation efficiency of $\sim 0.1\%$, a factor of 5 lower than measured previously at Aarhus, however to clean the moderator a long bake at low temperature (< 80 C) is required which was not possible during the beam time pressure. A short bake of 4 days, improved the moderator decay from 1.5 % per hour to 0.3-0.8 % per hour. Typically, positron traps with two nitrogen collision stages have a trapping efficiency of around 30 % (as was observed at the University of Aarhus for this system), hence we would expect around 40 k trapped positrons per second. The number of trapped positrons was measured to be 2.1 k per second, a factor of 20 lower than expected, or a trapping efficiency of only 1.5 %. We were able to measure the lifetime of the positrons in the trap with and without a rotating wall (RW) electric field (see fig 20A), which again was approximately 1 s and shows a roughly 7 times improvement with the RW, as opposed to without. The expansion rate was measured to be 5 mm/s (see fig. 20B).

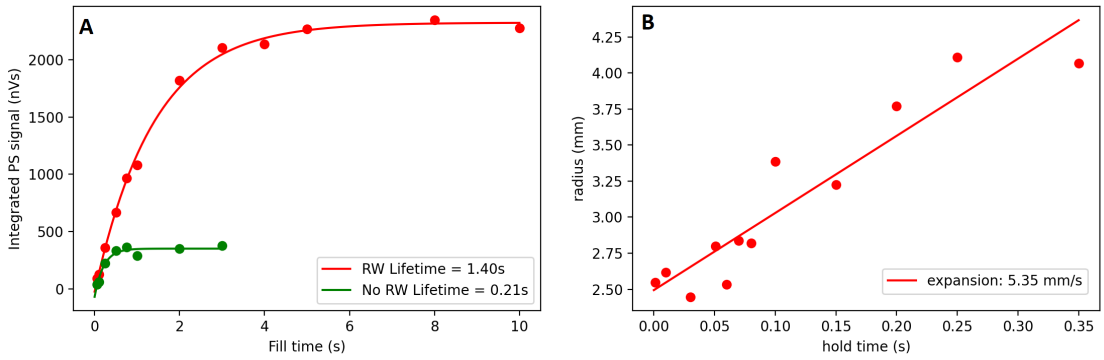

Figure 20 – A (LHS)– Comparison of positron lifetime with and without the rotating wall applied in the positron trap. B (RHS) – Measurement of the positron expansion rate in the FPS trap.

At present, this lower trapping efficiency is not understood. We are investigating possible problems with contamination in the gas handling system. If hydrocarbons are present this can cause a significant increase in the positron annihilation rate. New parts have been ordered to replace suspected problem equipment and will be tested shortly. Another major difference between the previous setup used at Aarhus and now at CERN is the pumping of the trap. As mentioned

above, replacing the broken cryopump with a turbo molecular pump (TMP) reduced the pumping speed for nitrogen by a factor of 4. We were able to source a replacement adsorber for the cryopump compressor which is now at CERN, and will be performing maintenance on the cold head to repair it for operation this year.

8.2 Positron accumulator

The positron accumulator was first installed last year [55] when testing with the previous positron trap was begun. To make space for the new slow-extracted antiproton beam experiments (see part III), the trap connections were moved to the upstream side of the apparatus early in April.

As the positron trap was under heavy development for most of the year, attempts were made to *breed* an electron plasma inside the accumulator to perform a first commissioning of the machine [61]. This is a technique where residual electrons in the vacuum are stochastically heated to the point that they can ionize the residual gases *breeding* an electron plasma, see fig 21. It was discovered that during this process one of the rotating wall electrode petals on C3 was floating, meaning that half of the trap was unavailable for use during catching. Although catching a single

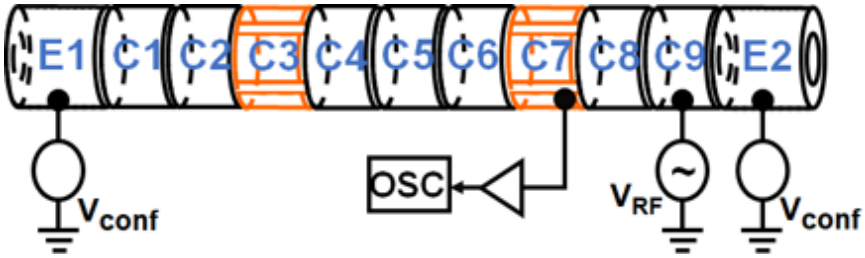

Figure 21 – Diagram of the positron accumulator electrode structure, showing an example of configuration used for *breeding* an electron plasma. An oscilloscope was attached to electrode C7 and heating RF applied on electrode C9.

stack in the trap was reported in 2021, this year we were able to demonstrate that catching multiple stacks of positrons was possible (see fig. 22B). Effective rotating-wall compression to a transverse cloud size below 5 mm was also observed. The filling was limited by a short positron lifetime in the accumulator ~ 10 s (see fig. 22A). Despite this short lifetime, we were able to successfully transfer positrons from the new accumulation stage to the Cusp trap on the last weekend of beam time. The number of positrons caught in the Cusp was unfortunately too low and time far too short for any mixing experiments.

Some initial investigations of the lifetime problem were made by transferring an electron plasma from the Cusp trap to the accumulator. In this case without any cooling gas, the electron lifetime was of the order of 100 s ideal for work within an ELENA cycle. It was only with the addition of cooling gas from the positron trap that the lifetime again reduced to < 1 s.

This has been an extremely difficult year for work with positrons, the phrase *'if anything can go wrong, it will'*, certainly rings true. In total during 2022 there were about 10 weeks that the system was operational for experiments. However, the required procedures for the operation of the positron system have been demonstrated. Positron beams are formed and they can be trapped. Multiple pulses were transferred from the trap to the accumulator. Finally positrons were transferred from the accumulator to the Cusp trap with minimal gas contamination as we can now isolate the trap.

There are three main problems at present: *i)* low moderation efficiency, which should be solved by a long baking period resulting in a factor of five improvement. *ii)* A factor of 20 reduction in trapping efficiency, for which we are investigating the pumping and gas systems, and checking

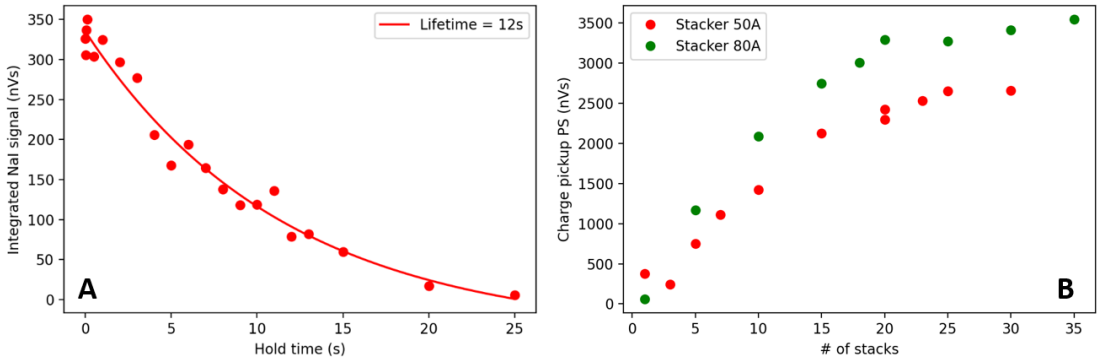

Figure 22 – A (LHS) – Lifetime of positrons stored in the accumulator with cooling gas present (P=2×10^{-7} mbar). B (RHS) – Comparison of filling the positron accumulator at two different magnetic field strengths.

trap alignment. *iii)* the low lifetime with gas present and shorted electrode in the accumulation stage. This problem has already being addressed to some extent in December. The electrode stack was removed and the shorted electrode fixed, and at the same time a 100 l/s TMP used in the accumulator system was replaced with an 800 l/s TMP which will improve the vacuum in this stage. Fixing the issues should provide a factor of around 100 times more positrons per pulse from the FPS trap or to put it another way around 210 k positrons per second and increase the lifetime in the accumulator, such that a high number of positrons can be stored. In an ELENA cycle that equates to about 20 million, with the new source from iThemba that number increases by another factor of 20.

9 Spectroscopy apparatus

9.1 Sextupole focusing magnet

In February, the superconducting Sextupole focusing magnet was moved from storage in Prevessin to the ASACUSA area for testing. The magnet required some work as pieces of equipment were missing, and control software needed to be updated as they had not been used for some time. The magnet was cooled to operational temperatures then energised. Previously the magnet had required many training cycles, however, in this case a maximum current of 400 A was reached after just three quenches. It was observed that at 400 A the temperature of the 'high temperature superconductor' feedthroughs got dangerously close to their maximum. This effect was not observed at 380 A or at 350 A, which was the current used to test the spectroscopy apparatus in the hydrogen beam setup (described in part IV).

The sextupole magnet uses a hybrid cooling system where the liquid helium bath for the magnet coils is cooled by a mechanical cryocooler to compensate for thermal losses when the system is cold. This way only a small amount of liquid helium is needed during the initial cooldown of the magnet, or a after a quench caused by e.g. a power failure.

9.2 Antihydrogen detector

In 2022 the antihydrogen detector underwent changes in its hardware and was transported back from Vienna to CERN, where it was reinstalled at the end of ASACUSA's beamline and first

measurements with cosmics and antiprotons were performed. After the previous hard- and software upgrades [62] the data acquisition only uses digital time-over-threshold (ToT) signals transferred to time-to-digital converters (TDCs).

The previous hodoscope fibre layers were replaced by scintillating tiles. As the detector consists of an outer and an inner layer of 32 bars each, the tiles have two different sizes. The outer tiles are $(129 \times 30 \times 5)$ mm^3 and the inner ones $(84 \times 20 \times 5)$ mm^3, see Figure 23. For each layer on each octagon segment 15 tiles are mounted on top of the existing four bars, perpendicular to them. Each tile is read out by two serially connected SiPMs on one side. By taking the signal coincidences of bars and tiles, it is now possible to get the hit coordinates in x, y and z direction with a resolution of (35×30) mm^2 on the outer and (20×20) mm^2 on the inner layer.

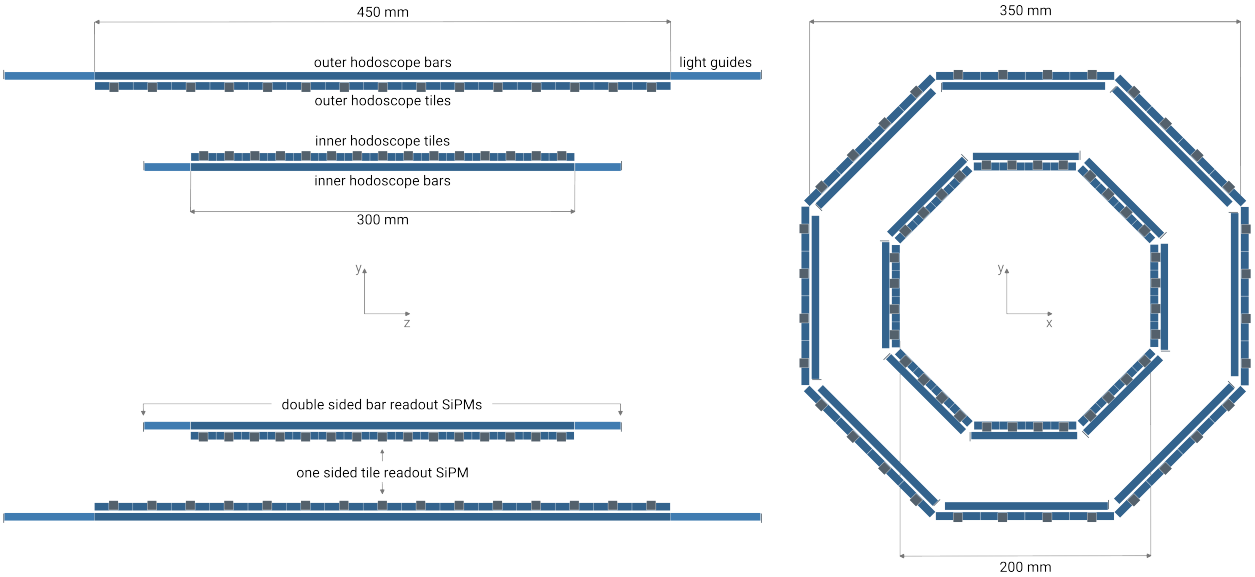

Figure 23 – Cross sections of the hodoscope in the y-z plane (left) and x-y plane (right) with their dimensions. The hodoscope bars with light guides and the new tile layers are shown including their readout SiPMs.

The readout of the central calorimeter, a BGO crystal scintillator [63], was performed using multi-channel photomultiplier tubes (PMTs). Since we need a data acquisition system capable of a detection rate up to 1 kHz the PMTs have been replaced by an array of 63 SiPMs mounted on the outside of the vacuum window, which is transparent to the light from the crystal. Charged particles traversing the BGO produce a light cone towards the SiPMs - hence several channels can be hit for each annihilation event.

Towards the end of this year's beam time antiprotons were slowly extracted to the BGO, see Sec. 7.1. Several thousand hits were recorded on the BGO in less than 500 ms. The beam shape and position is shown in the 2D histogram of Figure 24. In this extraction cycle over 22 000 hits were recorded. As this rate was still too high for our full data acquisition system, it was not possible at that time to calculate the corresponding antiproton annihilation events from the total number of counts.

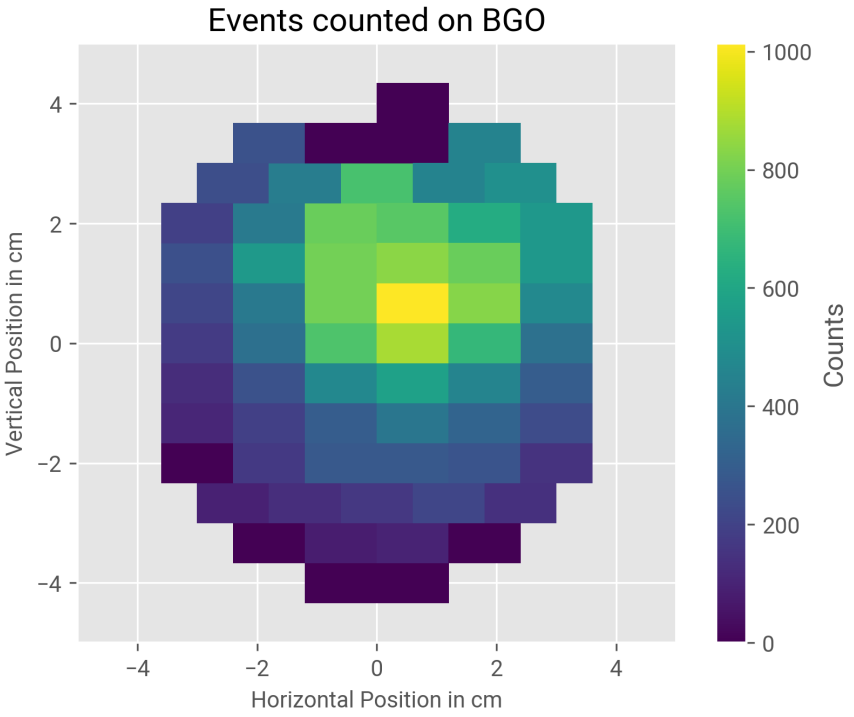

Figure 24 – Hit distribution of the over 22 000 hits on the BGO's SiPM channels recorded after one antiproton extraction.

10 Plans for 2023

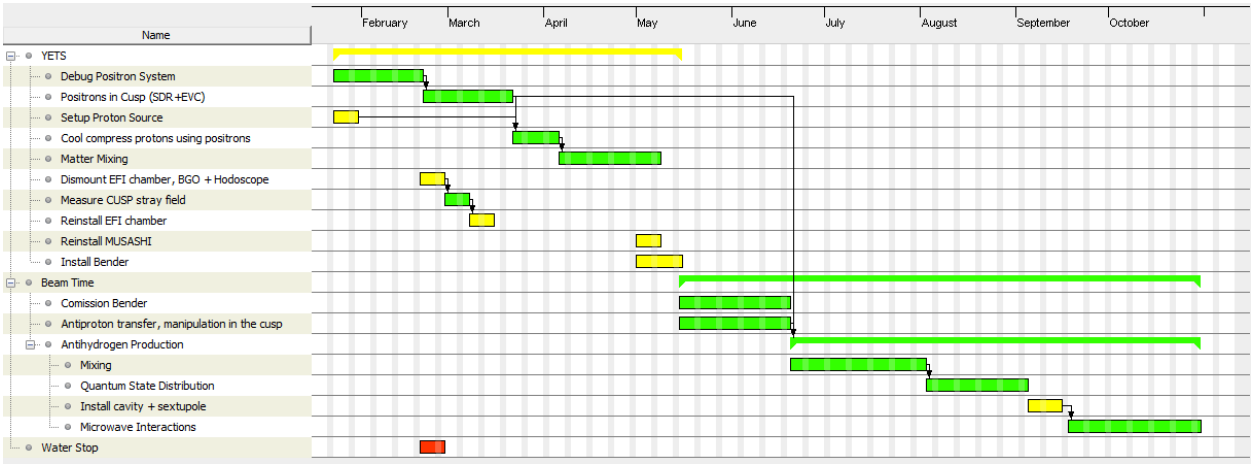

Figure 25 – Gantt Chart showing the preliminary schedule for 2023.

Fig. 25 shows the preliminary plan for the year 2023. We have to address before beam time the efficiency issues with the trap, the lifetime in the positron accumulator that were described above (Sec. 8). Once a large number of positrons are transferred to the Cusp they will have to be manipulated using the techniques that we have developed for electrons in previous years [56]. We have reinstalled the ASACUSA proton source [55] to perform matter mixing studies, which were delayed from LS2, and to continue beam development until antiprotons become available from mid-May. These studies also require a large number of positrons for cooling protons, so in the beginning of this year work on the positron system will be our absolute priority.

Measurements of the Cusp magnet stray field at the position of the cavity will be repeated in 2023, following issues with the readout in 2022. The new bender elements required for slow extraction studies (Part III) will be installed 2–4 weeks before beam time, and the first weeks of beam will be shared between studies of antiproton transfer to the Cusp trap and transport of antiprotons to the antiproton-nucleus collision region.

The majority of the beam time will be spent mixing and optimising the beam properties for spectroscopy. Later in the year we will install the cavity and sextupole and perform the first interaction between microwaves and the beam, which was delayed in 2022. Measurements of the quantum state distribution will be repeated to compare to previous work. We expect improvements in the intensity and ground state population, in line with predictions [64].

Part III
Study of annihilations with slow extracted antiprotons

1 Introduction

The first antiproton-nucleus ($\overline{\text{p}}$A) fragmentation measurements using very low-energy (<1 keV) antiprotons and thin targets (1–2 μm thickness) performed in ASACUSA [65,66], aimed to benchmark the different descriptions of $\overline{\text{p}}$ annihilation at rest. Charged pions and heavy fragments were detected using two detectors, Timepix3 quad [67] and the Hodoscope, described in sec 9.2. FLUKA [68] and Geant4 simulations (including two of the available models, FTF [69], and CHIPS [70]) have been completed and a publication is in preparation. The results suggest that the multiplicities of both minimum ionizing particles (MIPs) and heavily ionizing particles (HIPs) are best described by the FLUKA pre-equilibrium cascade (PEANUT) [71] model. The comparison of the deposited energies from the heavy fragments in data and simulations were challenging due to the so called "volcano" effect in the Timepix3 [72], which was partially overcome with the digitization of the simulations using an existing detector response model, Allpix^2 [73], and extending the code to take this effect into account.

A new extensive study was started during 2021 to measure $\overline{\text{p}}$A annihilation into charged particles for a representative set of light, medium-heavy and heavy nuclei. The goal is to produce data for tuning the Geant4 simulation and to explore some of the $\overline{\text{p}}$A process unknown traits, such as the Final State Interactions (FSI). The results are expected to be compared also to new calculations that extend the available Intranuclear Cascade of Liège (INCL) code [74] on $\overline{\text{p}}$A interactions.

1.1 Design and construction of beam optics elements for the transport of slow extracted antiprotons

According to the methods described in [55], the implementation of the $\overline{\text{p}}$A project is based on deflecting the slow extracted antiprotons from the MUSASHI trap by 90° and transporting them through the existing positron line to the annihilation target (see fig. 14). This requires various modifications and additions along the current beam line.

The beam optics simulations for the design of the different elements were performed in SIMION and included the full antiproton path from the trap to the target, taking into account the magnetic field of the solenoid and the transport coils. Different configurations were explored and the final design consisting of an electrostatic quadrupole deflector and three Einzel lenses was obtained via optimization routines, such as geometry sweep. The voltage settings for efficient antiproton transport were tuned using a Simplex optimizer and simulated annealing [75], whilst considering various shapes and sizes of the beam. The antiproton plasma after cooling and compression in the MUSASHI trap has a compressed component with ∼0.5 mm diameter and a halo component with ∼10 mm diameter [76,77]. Despite the presence of an extraction electrostatic lens that deflects the beam to suppress divergence at the exit of the MUSASHI trap, the halo component becomes too large to be focused again, so the beam transport optimization was concentrated on the compressed part. Fig. 26 shows a cross section of the simulated electrostatic parts with an exemplary beam, as well as x-y distribution of the input and the output beams.

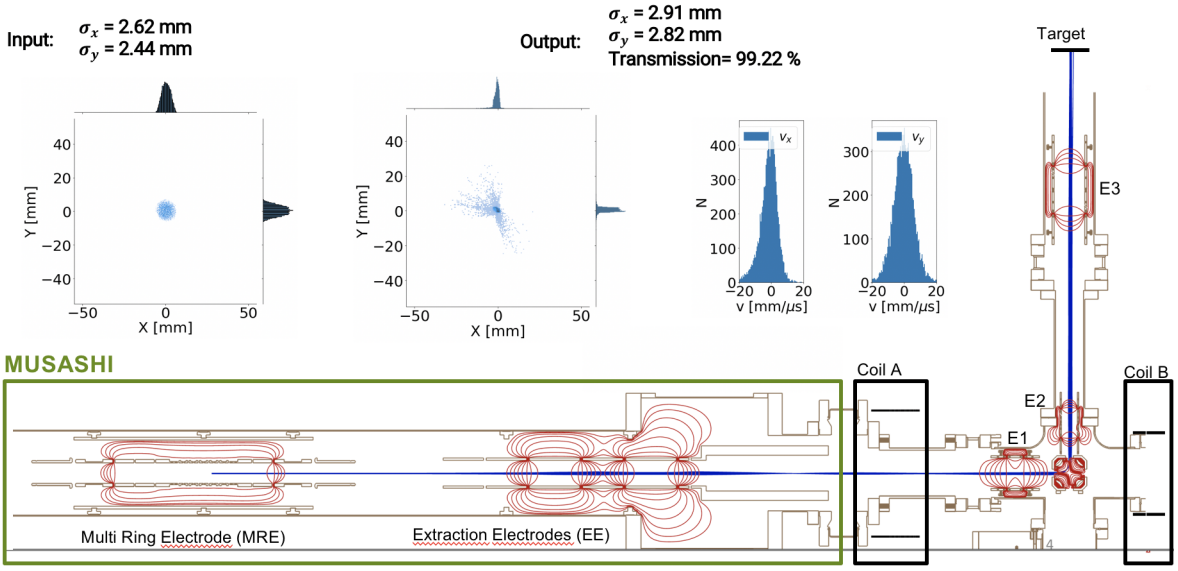

Figure 26 – **Bottom:** Cross-section of simulated electrostatic parts in SIMION with an exemplary beam. The position of the MUSASHI electordes, the transport coils, the einzel lenses (E1, E2 and E3) and the target is shown. **Top:** cross-sections of said beam just before E1 and at the expected position of the annihilation target (compressed part only from the initial plasma, see text). Histograms of the particle velocities, in X and Y direction are also given.

The design of the electrostatic system was finalised in summer 2022 and after an internal review the production of the various parts was finished in November. Fig. 27 shows a photograph of the actual quadrupole and the three Einzel lenses (E1, E2 and E3).

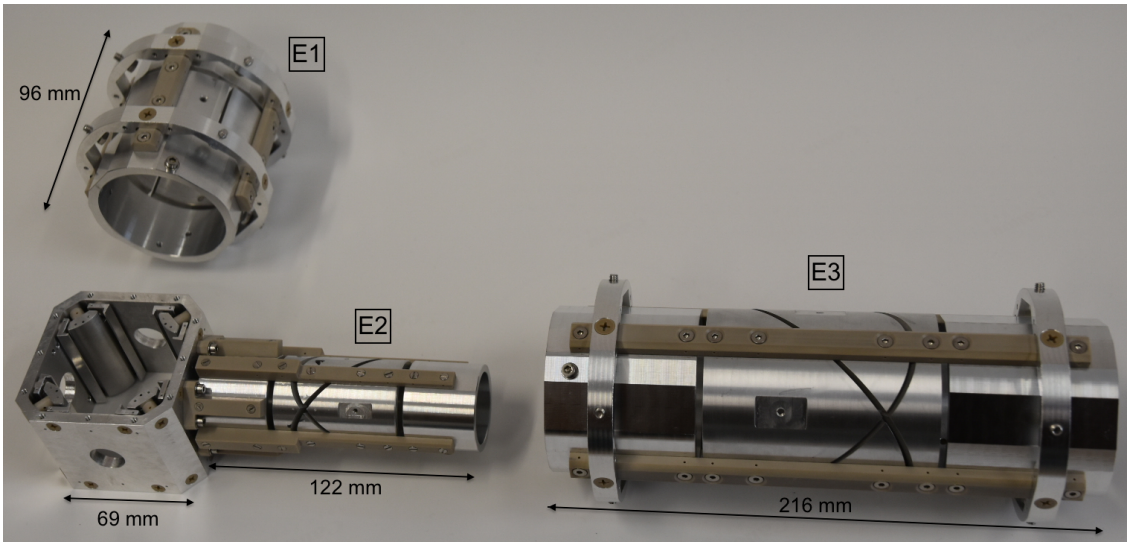

Figure 27 – Photograph of the electrostatic elements built for the antiproton transport from MUSASHI trap to the annihilation target.

E1 has a straight cut middle electrode for steering in X and Y direction, while the other two are Sikler-type einzel lenses that provide steering along any direction in the focal plane [78]. The quadrupole and E2 will be mounted on an UHV manipulator to allow for their insertion

and retraction without breaking the vacuum in the antiproton beamline. This will ensure an efficient switching between the antihydrogen spectroscopy and the annihilation measurements in the ASACUSA apparatus. The reduction of the overall beam time at CERN in 2022 and the delayes on the delivery of the manipulator didn't allow for enough time for installation and commissioning, and these milestones are expected to be achieved in the first weeks of beam time in 2023.

2 Detector development

2.1 Geant4 simulations

Simulations for the design of the detection system were performed in parallel with the work on the antiproton beam transport. As mentioned in [55], the detector will consist of Timepix3/Timepix4 ASICs coupled to thick (500 μm) silicon sensors, stacked in a cube-like formation and able to cover most of the 4π solid angle for the detection of the annihilation prongs.

Geant4 offers several physics lists, none of which was developed for simulating low energy antiproton annihilation. Hence different lists were investigated for the simulation of a 250 eV $\overline{\mathrm{p}}$ beam and the results were compared to select the optimal one. The results showed that not all antiprotons annihilate in the foil, but backscattering is a process with significant likelihood (∼50% according to the FTFP_BERT models). A previous study has reported the first experimental evidence for the reflection of antiprotons from solid surfaces (20 - 30% for the energies 1–10 keV) [79]. As these were never measured in sub-keV energy regime, this experiment will be able to measure whether backscattering is indeed important.

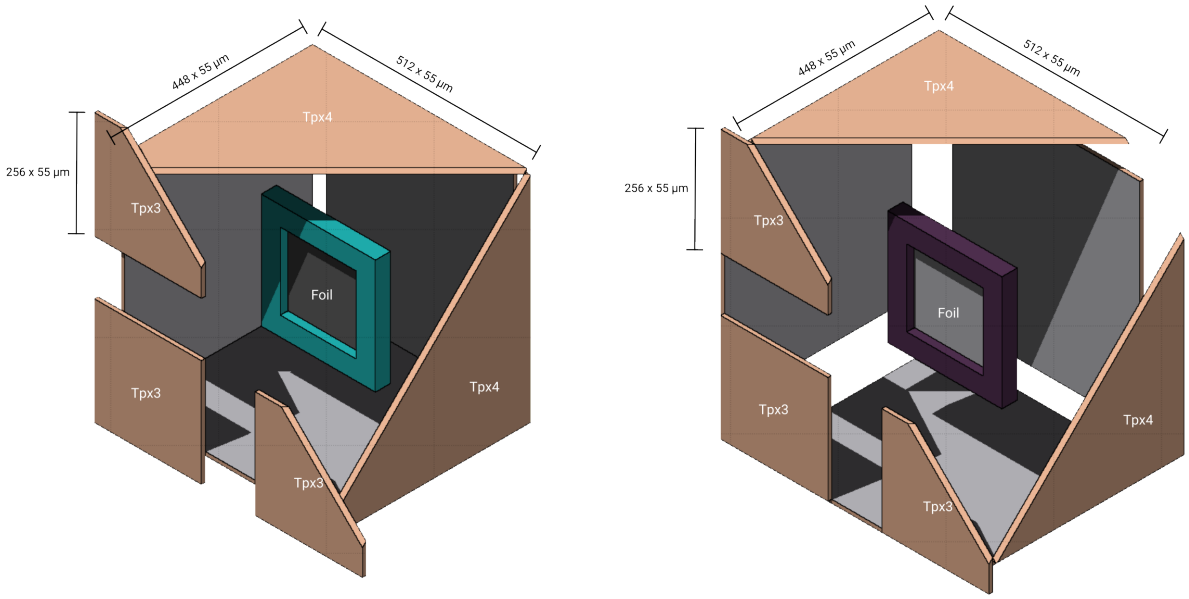

Figure 28 – Preliminary detector designs consisting of four Timepix3 detectors on the upstream side and five Timepix4 detectors surrounding a target foil at the center. The spaces between the Timepix3 allow a beam size up to 10 mm. The cut in the drawing was made for better visualisation. **Left:** Narrow geometry, where the space between the Timepix4 detectors was minimised. **Right:** Wide geometry, where the space between the Timepix4 detectors is larger, to allow for easier mounting of the target.

After identifying the most appropriate physics list (FTFP_BERT_EMZ), two cube-like geome-

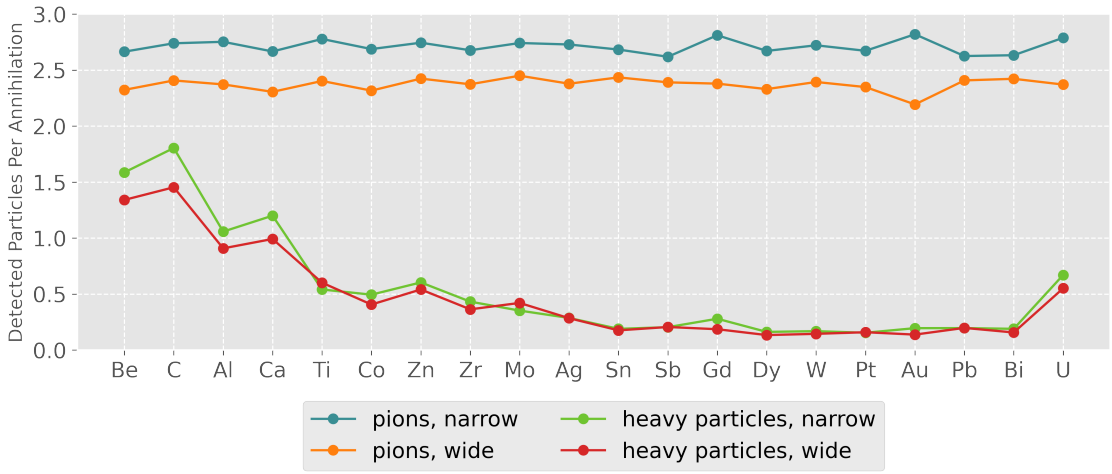

Figure 29 – Number of detected particles in the wide and narrow geometry for different foil materials, distinguishing between charged pions and heavier particles. This was simulated using Geant4 with the FTFP_BERT_EMZ physics list and an incoming beam of 250 eV antiprotons.

tries were simulated, consisting of five faces hosting Timepix4 detectors, while the side of the incoming beam is made of of four individual Timepix3 ASICs, with spaces between them to allow for the beam to reach the target. The two configurations are shown in fig. 28, one where the Timepix4 detectors are placed edge to edge ("narrow") and a second ("wide") with increased space between Timepix4 detectors to facilitate the mounting and changing of the foil target. The first covers $\sim 3.4\pi$ and the second $\sim 2.4\pi$ solid angle around the target foil for detection of the annihilation products. Both cases allow for a beam of 10 mm diameter to enter and hit the target.

Figure 29 shows the number of detected charged pions and heavier fragments (p, d, t, ^{3}He, ^{4}He etc.) per annihilation when implementing the wide and the narrow geometry. A tentative list of targets to be used in the measurements was selected, based on uniform distribution in the periodic system of elements and availability.

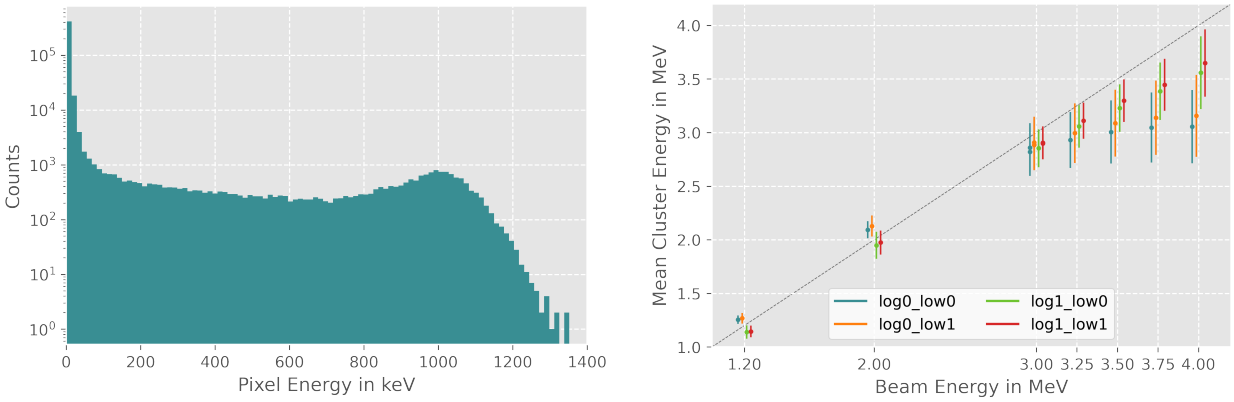

Figure 30 – **Left:** Histogram of the pixel energies in Timepix4 measured with a proton beam of 4 MeV. **Right:** The reconstructed proton beam energy from measurements with the same detector when applying different settings for the gain.

2.2 Timepix4 measurements with heavy ions

As mentioned in 1, the Timepix3 data showed the volcano effect which makes it difficult to analyse the energy deposit of heavier particles. The new Timepix4 chip is currently in development by the Medipix4 collaboration and a fully operational version will be available in summer 2023. The first version of this new ASIC together with the first prototype for its readout were assessed at the Vienna Environmental Research Accelerator (VERA) in March 2022, using proton (energies between 1-4 MeV) and carbon beams (10.8 MeV), which was the first-ever measurement using this new generation inside a vacuum system.
Besides the improved time resolution of only 200 ps which is crucial for the annihilation vertex reconstruction in this study, the Timepix4 also showed no volcano effect (see Fig. 30), with a dynamic range extending to >1 MeV without saturating, making it the preferred detector. After these measurements the detector was calibrated using test pulses and the results of the reconstructed energy of the incoming proton beam is shown in Fig. 30.

3 Plans for 2023

Two main lines of work can be identified: the transport of the antiproton beam to the target and the R&D for the detection system. What concerns the former, the electrostatic beam optics elements are going to be shipped to CERN in late March, after the actuator for the automatic insertion of the quad is delivered. The installation will take place in the first two weeks of May and the commissioning will start from mid-May, i.e. as soon as antiprotons are available again (see fig. 25.

For the detector, a new design of the PCB for Timepix4 that will allow stacking in a cube-like configuration is being negotiated with NIKHEF (Amsterdam), to be prepared before the Timepix4 ASICs become available, which should happen in summer 2023. The design of the whole system is expected to also be finished by then. Bump bonding to the silicon sensors and wire bonding to the PCB is planned to be done in early autumn, after which laboratory tests of each individual detectors can be performed. The again reduced beam time in 2023 will very likely shift the data taking to the next year, in which case we will perform a set of measurements at VERA with heavy ions. A detailed study of the signal coming from different ions is required for developing algorithms for particle identification of the prongs from the antiproton annihilation.

If beam time permits, a new set of data can be taken with the Timepix3 quad (used for the previous measurements, see sec. 1) with titanium and beryllium targets.

Part IV
Experiments with hydrogen beams

In parallel to the antihydrogen setups, ASACUSA has constructed and operated matter experiments for the purpose of *i)* commissioning and validating the Rabi-type spectroscopy method proposed for antihydrogen with hydrogen beams [80], *ii)* matter experiments able to constrain SME coefficients without comparison to antimatter [81–83], and *iii)* developing methods to de-excite Rydberg hydrogen atoms produced in the three-body recombination process. The latter is a joint activity with the AEgIS collaboration.

In 2022 the experimental tasks of *i)* and *ii)* have been completed at CERN. The atomic hydrogen beamline as shown in figure 31 was deconstructed. All parts except device (f) have been shipped to the Laboratoire Aimé Cotton, Université Paris-Saclay in October 2022, where it will be deployed to perform for instance experiments on deuterium.

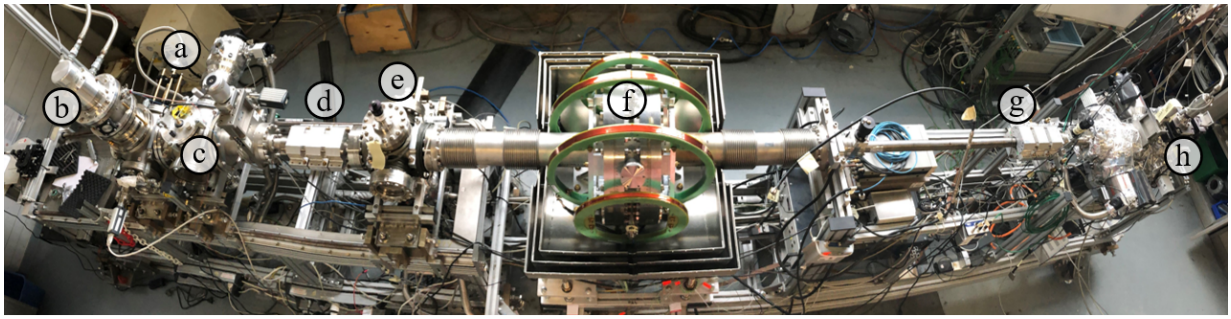

Figure 31 – Photograph of the atomic hydrogen beam experiment at Bat. 275 in 2022 before deconstruction: (a) H_2-supply and dissociation plasma tube (b) coldhead for cooling of H (c) chopper wheel to modulate the beam for ToF measurements and background suppression (d) sextupole magnets for beam polarisation (e) helical beam blocker for two-dimensional beam profile measurements (f) cavity-assembly consisting of a stripline cavity, surrounded by McKeehan-like coils and three layers of magnetic shielding (g) sextupole magnets for spin state analysis (h) quadrupole mass spectrometer for H-ionisation and mass-selective counting of protons.

1 Commissioning of ASACUSAs hyperfine spectrometer

From 2013 to 2015 the hydrogen beam was operated at the CERN cryolab, where the superconducting sextupole magnet and a cavity-assembly for the σ transition ($F, M_F : 1, 0 \rightarrow 0, 0$) have been tested successfully [80, 84]. The superconducting sextupole magnet was installed at the AD during antiproton runs in 2015 and 2016, however, the antihydrogen beam rates have been too low for hyperfine spectroscopy. While focusing on improving the beam production the superconducting sextupole magnet was stored. In 2022 it has been recommissioned successfully (see I 9.1).

Over the last seven years the hydrogen beam has been located at Bat. 275 with a focus on the improved cavity-assembly, which is shown in figure 31(f). With this device it is possible to investigate the more sensitive π transition ($F, M_F : 1, 1 \rightarrow 0, 0$) in addition to the σ transition. The measurements with hydrogen performed with this setup revealed that the operation in the optimal B-field environment will be beneficial for the hyperfine experiment. At too low magnetic fields around 1 μT the σ and π transition start interfering and fitting the observed line shapes becomes increasingly difficult. Whereas if higher magnetic fields approaching 1 mT are produced

the inhomogeneities scale up accordingly and lead to asymmetric lineshapes. Those effects are now well understood owing to the ongoing in-depth analysis of the experiment sketched in the next section. However, for the first measurements with antihydrogen it is advisable to stay in the intermediate regime, where the observed line shapes are symmetric as expected under ideal conditions.

Therefore, in 2022 a set of measurements of σ and π transition at a field of 23 μT (corresponding to a current of 100 mA on the McKeehan-like coils) have been performed to conclude the tests with hydrogen. This is now the proposed field value to start antihydrogen spectroscopy at as soon as a sufficiently intense beam can be produced. A detailed analysis of this ultimate data set will benefit from the insights gained during the more complex analysis of the data taken at higher magnetic fields for independent SME tests. For this reason it will be worked on subsequently and a final result is therefore not yet available but expected to follow early 2023.

The importance of the static magnetic field also calls for comprehensive measurements of the magnetic field environment of the ASACUSA AD zone. The most notable difference to the test measurements with hydrogen at Bat. 275 is the presence of the stray field of the double CUSP magnet. Field measurement performed in 2022 have to be repeated this year due to a sensor problem. Based on these measurements field compensation coils will be buil in 2023.

2 Hydrogen hyperfine spectroscopy at magnetic fields close to 1 mT

From January to May 2022 measurements were performed at ASACUSA's hydrogen beamline at CERN with the goal to set limits on yet unconstrained SME coefficient. The principal idea is, that conventional sidereal variation measurements are only sensitive to two of the three space dimensions. By swapping the magnetic field direction in our experiment we become sensitive to the third direction, which has not been probed by hydrogen maser measurements relying on the conventional sidereal variation method [85]. The difficulty is to guarantee, that the swapped magnetic fields actually have the same absolute value. We therefore use the σ transition as a reference. This transition with ΔM_F=0 remains unaffected even in CPT or Lorentz invariance broken scenarios of the SME. Strictly speaking this is only correct at zero magnetic field, however, at the present field values potential effects will remain strongly suppressed for the σ transition. The operation at relatively high fields is motivated by the fact, that the field sensitivity of the σ transition gets enhanced. In those measurements π and σ transitions are repeatedly measured sequentially and at opposite magnetic field orientations. Such data has been taken at three different magnetic fields as summarized in table 1.

Coil current	Magnetic field	Number of resonance-pairs measured
± 2.0 A	± 460 μT	200
± 2.5 A	± 575 μT	506
± 3.0 A	± 690 μT	408

Table 1 – Overview on the data sets taken in 2022 for constraining SME coefficients not covered by sidereal variation measurements using hydrogen masers [85].

To avoid any bias the data was blinded. The fitting function had to be extended to include effects stemming from inhomogeneities of the static magnetic field, which become more prominent at the stronger fields used for this investigation. From earlier magnetic field measurements with fluxgate

sensors it was known, that in beam direction a small systematic field dependence of parabolic shape exists. In planes perpendicular to the beam direction the field distribution was considerably smaller compared to the parabolic change in beam direction. First a static magnetic field with a parabolic dependence in beam direction was implemented in the numeric code solving the von Neumann equation of the four level system. This improvement can account for asymmetries in the observed rate spectra. Next the comparatively smaller distribution of field values in the planes perpendicular to the beam direction were implemented as a statistical broadening or smearing of the resonance line shape. The effect of these corrections is exemplified in figure 32, where fits with and without inclusion of these effects are used on the same data of a π transition. This shows that both effects need to be implemented to achieve convincing fit results.

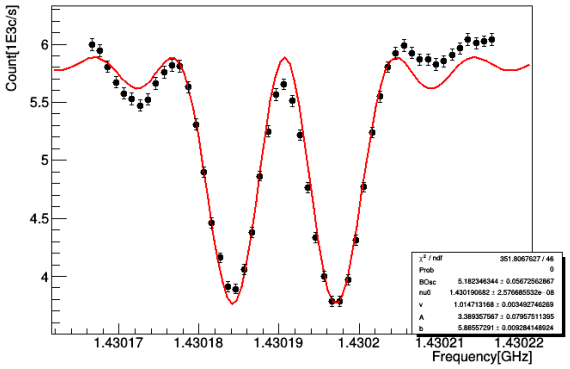

(a) Fit of a rate spectrum for a π transition at high magnetic fields ($\approx$690 μT) assuming a perfectly homogeneous static magnetic field. The line shape of the fit is symmetric and deviates systematically from the observed rates.

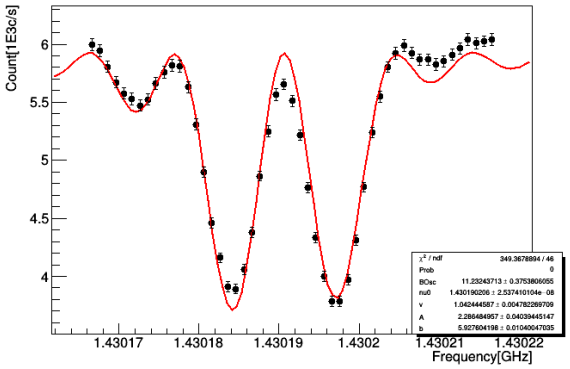

(b) Same data as in (a) now using a fit function, which considers a systematically (parabolic) changing field seen by the hydrogen atoms traversing the microwave cavity. This effect enables to explain asymmetric rate spectra, but further systematic deviations are still visible.

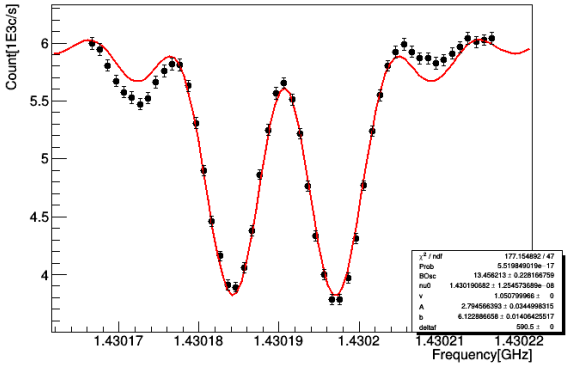

(c) Same data as in (a) now using a fit function, which accounts for statistical field changes in the plane perpendicular to the beam direction. This effect can resemble a reduced rate at the central maximum, however it can't account for asymmetries.

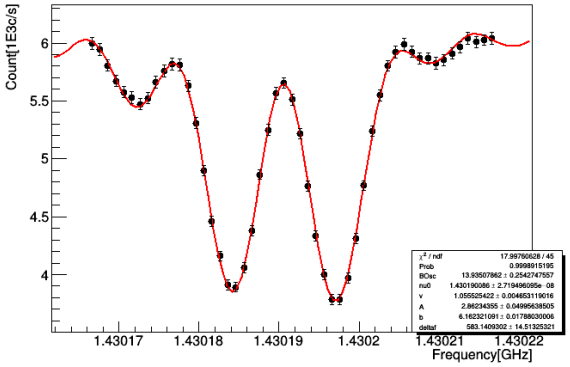

(d) Same data as in (a) now using a fit, which accounts for both effects as included in (b) and (c). With this combination convincing fit results are achieved.

Figure 32 – Demonstration of the improvement of the fit function by successively incorporating effects caused by inhomogeneities of the static magnetic field. Assuming a perfectly uniform magnetic field yields the bad fit result of (a). The systematically changing field in beam direction can account for asymmetries (b) and the field distributions in planes perpendicular to the beam explain a statistical broadening (c). Convincing fit results are achieved if both effects are included (d).

3 Excited hydrogen beam

This experimental activity aims to stimulate the decay of highly excited $\overline{\mathrm{H}}$ states that are formed at the production point inside the cusp trap. Our previous simulation work [86] showed that the high angular momentum and long radiative lifetimes of the initially produced states, hinder efficient in-beam ground-state hyperfine spectroscopy. Following theoretical work on stimulated deexcitation techniques [87, 88], a proof-of-principle experiment was conducted to examine the potential of different light sources for stimulating the deexcitation of high-lying Rydberg states. This work, published in 2021, demonstrated the successful use of photomixers to induce stimulated THz transitions between Rydberg states in Cesium atoms [89]. Building upon this work, studies on hydrogen was initiated at CERN in 2020 with the goal of demonstrating fast stimulated deexcitation to the ground state before applying the technique to the $\overline{\mathrm{H}}$ setup. Characterisation measurements on hydrogen from plasma sources carried out in 2020 were followed by the construction of a dedicated laser lab in building 275, containing a hydrogen beam experiment coupled to a laser for exciting the hydrogen atoms into the Rydberg states, so that deexcitation studies can be performed.

This experimental setup uses a microwave-powered plasma to dissociate molecular hydrogen and produce a beam of thermal hydrogen atoms. The beam is then emitted through a pinhole aperture into a downstream vacuum. Following the commissioning of the hydrogen beamline at the end of 2021, research was conducted on the formation of Rydberg states through collissional excitation within the plasma formation region using electric field ionization, as published in Ref. [90]. Further characterisation of Rydberg formation from the plasma source was continued in the first quarter of 2022. Due to low statistics and the sensitivity of the Rydberg population to the conditions in the hydrogen formation region it was decided to focus on laser excitation to generate Rydberg states.

An injection-seeded Ti:Sa laser system was commissioned in late 2021 for exciting hydrogen atoms from the 2s state to Rydberg states. The laser consists of a commercial Nd:YAG laser that generates pulses of light at a wavelength of 523 nm, which is frequency doubled and fed into a gain-switched Ti:Sa cavity. The cavity is seeded with a continuous-wave Sacher TEC520 diode laser. The output of the cavity is then frequency doubled using a Beta-barium borate (BBO) crystal to produce pulses of light at a wavelength of 364 nm. After further optimisation in 2022, the laser was able to generate average pulse energies of up to 20 mJ, which was more than sufficient to saturate the transitions to the Rydberg states of interest. The stability issues with the laser were resolved by gating out Q-switch interference from the diode signal used for locking the laser cavity.

To access transitions from the metastable $2s$ state to longer-lived circular levels, a region with crossed magnetic and electric fields is necessary. Based on the technique described in Ref. [91], a crossed electric and magnetic field region was adapted for use with hydrogen atoms. The cross-field region consists of two parallel plate electrodes placed on either side of the hydrogen beam within a homogeneous magnetic field region generated by two Helmholtz coils. Laser excitation of hydrogen atoms occurs when the combination of electric and magnetic fields mixes the quantum states. The electric field is gradually reduced to maintain adiabatic transfer into the circular state. In a first measurement campaign in the summer of 2022, we attempted to excite $2s$ states emitted directly from the plasma through collisional deexcitation processes. However, we were unable to observe a clear excitation signal, likely due to stray field quenching of the $2s$ states near the plasma formation region.

As an alternative approach to forming 2s states, a beam-foil technique was used [92]. To implement this method, a pulsed proton source was constructed using a high-voltage pulser electrode placed near the dissociation plasma. This generated a pulse of protons with energies up to 500 eV, which was sufficient to penetrate a 12 nm thick carbon foil provided to us by the GBAR collaboration. However, we encountered difficulties in controlling the discharge current at the few tenths

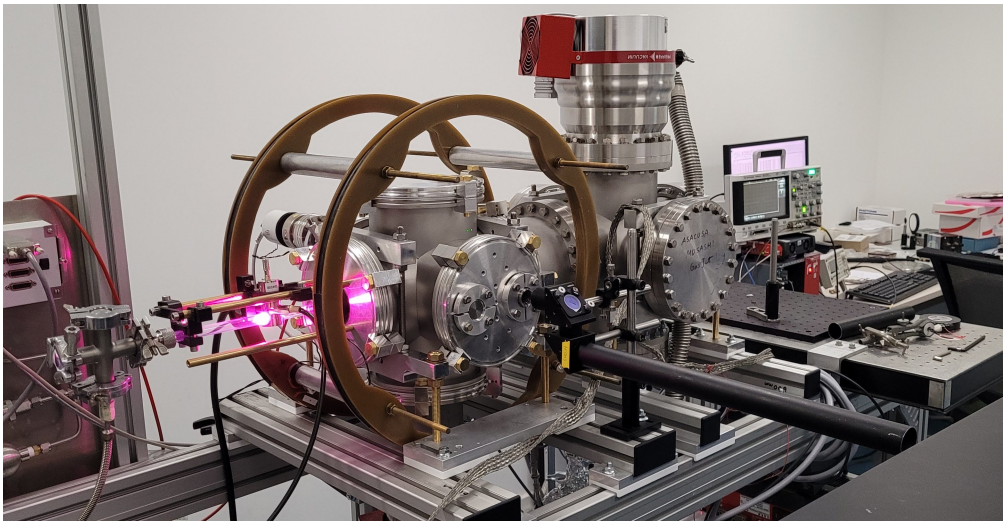

Figure 33 – Photograph of the hydrogen deexcitation setup. Molecular hydrogen is dissociated within a microwave discharge plasma (pink glow). The magnetic field for the cross-field region is generated by two Helmholtz coils, laser light for excitating into the circular Rydberg states is sent into the chamber through a side viewport. The quantum state distribution of the emitted atomic beam is probed in the most downstream chamber using a tunable electric field. The ionization products are detected with microchannel plate detectors.

of mbar needed to maintain the hydrogen discharge plasma, resulting in the beam from the source rupturing the foil. These studies are ongoing, and we are considering using an electron gun source to excite the hydrogen beam or a two-photon 248 nm transition from the ground state.

While the hydrogen excitation campaign was ongoing, we also conducted experimental studies on different potential sources of Rydberg state mixing light. THz power measurements of various filtered sources of black-body radiation were performed by a summer student and showed that a 12 W hot-wire lamp generated roughly 2 mW of output at frequencies below 5 THz, after unwanted radiation was filtered out using polyethylene foils. In collaboration with a CNRS group led by Jean-Francois Lamping at Lille, we found that porous teflon filters combined with polyethylene film worked well as a bandpass filter for wavelengths below 3 THz. Additionally, we initiated the development of dedicated photomixers for THz light and explored different techniques for transporting THz light into the experimental region of an antimatter experiment.

4 Plans for 2023

The hydrogen hyperfine spectroscopy measurements performed at CERN have provided important insights for the forthcoming antihydrogen in-beam spectroscopy measurements; allowing to determine the optimal static field configuration and precisely study effect of inhomogeneities on the line shape structure. As scheduled last year, the hydrogen beamline has been dismantled in October 2022 and the cavity, shielding and associated hardware have now been transported to the AD in preparation for antihydrogen spectroscopy. The rest of the beamline has been transported to the Laboratoire Aimé Cotton in Paris where further measurements on hydrogen and deuterium will be performed. The analysis of the latest data collected at CERN with this hydrogen beamline is ongoing. We foresee unblinding of the data in the coming weeks. The results will provide first constrains on yet unconstrained SME coefficients at an expected precision level of $\sim 3 \cdot 10^{-22}$ GeV.

Work on the second hydrogen line dedicated to deexcitation studies will be pursued in 2023 with the target of finalising the assessment of different light sources performance in stimulating the decay of Rydberg states.

References

[1] A. Sótér, H. Aghai-Khozani, D. Barna, A. Dax, L. Venturelli, and M. Hori, *Nature*, vol. 603, pp. 411–415, 2022.

[2] M. Hori, A. Sótér, and V. I. Korobov, *Phys. Rev. A*, vol. 89, p. 042515, 2014.

[3] M. Hori, H. Aghai-Khozani, A. Sótér, A. Dax, and D. Barna, *Nature*, vol. 581, p. 37, 2020.

[4] Z.-D. Bai, V. I. Korobov, Z.-C. Yan, T.-Y. Shi, and Z.-X. Zhong, *Phys. Rev. Lett.*, vol. 128, p. 183001, 2022.

[5] V. I. Korobov, L. Hilico, and J.-P. Karr, *Phys. Rev. Lett.*, vol. 112, p. 103003, 2014.

[6] V. I. Korobov, L. Hilico, and J. -P. Karr, *Phys. Rev. A*, vol. 89, p. 032511, 2014.

[7] V. I. Korobov, *Phys. Rev. A*, vol. 89, p. 014501, 2014.

[8] V. I. Korobov, A. K. Bekbaev, D. T. Aznabayev, and S. A. Zhaugasheva, *J. Phys. B*, vol. 48, p. 245006, 2015.

[9] M.-H. Hu *et al.*, *Chem. Phys. Lett.*, vol. 654, p. 114, 2016.

[10] F. Ficek *et al.*, *Phys. Rev. Lett.*, vol. 120, p. 183002, 2018.

[11] D. Baye, J. Dohet-Eraly, and P. Schoofs, *Phys. Rev. A*, vol. 99, p. 022508, 2019.

[12] T. P. Grozdanov and E. A. Solov'ev, *Eur. Phys. J. D*, vol. 74, no. 3, p. 50, 2020.

[13] Z.-D. Bai, Z.-X. Zhong, Z.-C. Yan, and T.-Y. Shi, *Chin. Phys. B*, 2021.

[14] M. Hori *et al.*, *Phys. Rev. Lett.*, vol. 96, p. 243401, 2006.

[15] T. Pask *et al.*, *Phys. Lett. B*, vol. 678, p. 55, 2009.

[16] M. Hori *et al.*, *Nature*, vol. 475, p. 484, 2011.

[17] T. Kobayashi *et al.*, *J. Phys. B*, vol. 46, p. 245004, 2013.

[18] S. Friedreich *et al.*, *J. Phys. B*, vol. 46, p. 125003, 2013.

[19] M. Hori *et al.*, *Science*, vol. 354, p. 610, 2016.

[20] A. Adamczak and D. Bakalov, *Phys. Rev. A*, vol. 88, p. 042505, 2013.

[21] A. Adamczak and D. Bakalov, *Phys. Rev. A*, vol. 90, p. 054501, 2014.

[22] M. Hori *et al.*, *Phys. Rev. Lett.*, vol. 89, p. 093401, 2002.

[23] M. Hori *et al.*, *Phys. Rev. Lett.*, vol. 87, p. 093401, 2001.

[24] M. Hori, K. Yamashita, R. S. Hayano, and T. Yamazaki, *Nucl. Instr. Meth. Phys. Res. A*, vol. 496, p. 102, 2003.

[25] M. Hori *et al.*, *Phys. Rev. A*, vol. 70, p. 012504, 2004.

[26] H. Yamaguchi *et al.*, *Phys. Rev. A*, vol. 66, p. 022504, 2002.

[27] H. Yamaguchi *et al,*, *Phys. Rev. A*, vol. 70, p. 012501, 2004.

[28] M. Hori and A. Dax, *Opt. Lett.*, vol. 34, p. 1273, 2009.

[29] D. Bakalov, B. Jeziorski, T. Korona, K. Szalewicz, and E. Tchoukova, *Phys. Rev. Lett.*, vol. 84, p. 2350, 2000.

[30] D. Bakalov, *Hyperfine Interact.*, vol. 209, pp. 25–28, 2012.

[31] T. Aramaki *et al.*, *Astropart. Phys.*, vol. 74, pp. 6–13, 2016.

[32] F. Nozzoli, F. Dimiccoli, R. Iuppa, E. Riccia, and P. Zuccona, "An helium calorimeter for antideuteron identification in cosmic rays," in *Proc. 37th International Cosmic Ray Conf.(ICRC2021)(IUPAP, 2021)*, 2021.

[33] M. Hori and V. I. Korobov, *Phys. Rev. A*, vol. 81, p. 062508, 2010.

[34] V. Chohan *et al.*, "Extra Low ENergy Antiproton ring (ELENA) and its transfer lines, design report," CERN-2014-002 (CERN, Geneva), 2014.

[35] D. Gamba *et al.*, "ELENA commissioning," in *Proceedings of North American Particle Accelerator Conference NAPAC2019, Lansing MI, USA*, 2019, p. WEYBB1.

[36] M. Hori, *Review of scientific instruments*, vol. 76, no. 11, p. 113303, 2005.

[37] K. Nordlund, M. Hori, and D. Sundholm, *Phys. Rev. A*, vol. 106, no. 1, p. 012803, 2022.

[38] C. J. Batty, E. Friedman, and A. Gal, *Nucl. Phys. A*, vol. 689, p. 721, 2001.

[39] A. Bianconi, M. Corradini, A. Cristiano, M. Leali, E. L. Rizzini, L. Venturelli, N. Zurlo, and R. Donà, *Phys. Rev. A*, vol. 78, p. 022506, 2008.

[40] A. Bianconi *et al.*, *Phys. Lett. B*, vol. 704, p. 461, 2011.

[41] H. Aghai-Khozani *et al.*, *Eur. Phys. J. Plus*, vol. 127, p. 125, 2012.

[42] M. Corradini *et al.*, *Nucl. Instrum. Meth. A*, vol. 711, p. 12, 2013.

[43] A. Sótér *et al.*, *Rev. Sci. Instrum.*, vol. 85, p. 023302, 2014.

[44] K. Todoroki *et al.*, *Nucl. Instrum. Meth. A*, vol. 835, p. 110, 2016.

[45] H. Aghai-Khozani *et al.*, *Nucl. Phys. A*, vol. 970, p. 366, 2018.

[46] H. Aghai-Khozani *et al.*, *Nucl. Phys. A*, vol. 1009, p. 122170, 2021.

[47] M. Hori, *Nucl. Instrum. Meth. A*, vol. 522, no. 3, p. 420, 2004.

[48] K. Nordlund, *Comput. Mater. Sci.*, vol. 3, no. 4, p. 448, 1995.

[49] K. Nordlund, D. Sundholm, P. Pyykkö, D. M. Zambrano, and F. Djurabekova, *Phys. Rev. A*, vol. 96, no. 4, p. 042717, 2017.

[50] A. Lühr and A. Saenz, *Phys. Rev. A*, vol. 79, no. 4, p. 042901, 2009.

[51] J. J. Bailey, A. S. Kadyrov, I. B. Abdurakhmanov, D. V. Fursa, and I. Bray, *Phys. Rev. A*, vol. 92, no. 2, p. 022707, 2015.

[52] A. Bianconi, G. Bonomi, E. L. Rizzini, L. Venturelli, and A. Zenoni, *Phys. Rev. C*, vol. 62, no. 1, p. 014611, 2000.

[53] K. Protasov, G. Bonomi, E. Lodi Rizzini, and A. Zenoni, *Eur. Phys. J. A*, vol. 7, no. 3, p. 429, 2000.

[54] E. Klempt, F. Bradamante, A. Martin, and r. Richard, *Phys. Rep.*, vol. 368, no. 2-3, pp. 119–316, 2002.

[55] M. Hori and E. Widmann, "Status report of the ASACUSA experiment - progress in 2021 and plans for 2022," CERN, Geneva, Tech. Rep., 2022. [Online]. Available: https://cds.cern.ch/record/2799130

[56] C. Amsler, H. Breuker, S. Chesnevskaya, G. Costantini, R. Ferragut, M. Giammarchi, A. Gligorova, G. Gosta, H. Higaki, E. D. Hunter, C. Killian, V. Kletzl, V. Kraxberger, N. Kuroda, A. Lanz, M. Leali, V. Mäckel, G. Maero, C. Malbrunot, V. Mascagna, Y. Matsuda, S. Migliorati, D. J. Murtagh, Y. Nagata, A. Nanda, L. Nowak, E. Pasino, M. Romé, M. C. Simon, M. Tajima, V. Toso, S. Ulmer, L. Venturelli, A. Weiser, E. Widmann, T. Wolz, Y. Yamazaki, and J. Zmeskal, "Reducing the background temperature for cyclotron cooling in a cryogenic penning–malmberg trap," *Physics of Plasmas*, vol. 29, no. 8, p. 083303, 2022.

[57] N. Kuroda, S. Ulmer, D. J. Murtagh, S. Van Gorp, Y. Nagata, M. Diermaier, S. Federmann, M. Leali, C. Malbrunot, V. Mascagna, O. Massiczek, K. Michishio, T. Mizutani, A. Mohri, H. Nagahama, M. Ohtsuka, B. Radics, S. Sakurai, C. Sauerzopf, K. Suzuki, M. Tajima, H. A. Torii, L. Venturelli, B. Wünschek, J. Zmeskal, N. Zurlo, H. Higaki, Y. Kanai, E. Lodi Rizzini, Y. Nagashima, Y. Matsuda, E. Widmann, and Y. Yamazaki, *Nat Commun*, vol. 5, Jan. 2014.

[58] N. Kuroda, H. A. Torii, Y. Nagata, M. Shibata, Y. Enomoto, H. Imao, Y. Kanai, M. Hori, H. Saitoh, H. Higaki, A. Mohri, K. Fujii, C. H. Kim, Y. Matsuda, K. Michishio, Y. Nagashima, M. Ohtsuka, K. Tanaka, and Y. Yamazaki, "Development of a monoenergetic ultraslow antiproton beam source for high-precision investigation," *Physical Review Special Topics - Accelerators and Beams*, vol. 15, no. 2, pp. 1–10, 2012.

[59] Costantini, Giovanni, Giorleo, Luca, Gosta, Giulia, Leali, Marco, Mascagna, Valerio, Migliorati, Stefano, Prest, Michela, Ronchetti, Federico, Solazzi, Luigi, Vallazza, Erik, and Venturelli, Luca, "Upgrade of the scintillating bars detector for the asacusa experiment," *EPJ Web Conf.*, vol. 262, p. 01013, 2022. [Online]. Available: https://doi.org/10.1051/epjconf/202226201013

[60] M. Hori and E. Widmann, "ASACUSA PROPOSAL FOR ELENA," CERN, Geneva, Tech. Rep. CERN-SPSC-2019-035. SPSC-P-307-ADD-2, Oct 2019. [Online]. Available: http://cds.cern.ch/record/2691506

[61] G. Maero, S. Chen, R. Pozzoli, and M. Romé, "Low-power radio-frequency excitation as a plasma source in a penning–malmberg trap: a systematic study," *Journal of Plasma Physics*, vol. 81, no. 5, p. 495810503, 2015.

[62] V. Kraxberger, C. Amsler, H. Breuker, S. Chesnevskaya, G. Costantini, R. Ferragut, M. Giammarchi, A. Gligorova, G. Gosta, H. Higaki, E. Hunter, C. Killian, V. Kletzl, N. Kuroda, A. Lanz, M. Leali, V. Mäckel, G. Maero, C. Malbrunot, V. Mascagna, Y. Matsuda, S. Migliorati, D. Murtagh, Y. Nagata, A. Nanda, L. Nowak, E. Pasino,

M. Romé, M. Simon, M. Tajima, V. Toso, S. Ulmer, L. Venturelli, A. Weiser, E. Widmann, T. Wolz, Y. Yamazaki, and J. Zmeskal, "Upgrade of asacusa's antihydrogen detector," *Nuclear Instruments and Methods in Physics Research Section A: Accelerators, Spectrometers, Detectors and Associated Equipment*, vol. 1045, p. 167568, 2023. [Online]. Available: https://www.sciencedirect.com/science/article/pii/S0168900222008609

[63] Y. Nagata, N. Kuroda, B. Kolbinger, M. Fleck, C. Malbrunot, V. Mäckel, C. Sauerzopf, M. Simon, M. Tajima, J. Zmeskal, H. Breuker, H. Higaki, Y. Kanai, Y. Matsuda, S. Ulmer, L. Venturelli, E. Widmann, and Y. Yamazaki, "Monte-carlo based performance assessment of asacusa's antihydrogen detector," *Nuclear Instruments and Methods in Physics Research Section A: Accelerators, Spectrometers, Detectors and Associated Equipment*, vol. 910, pp. 90–95, 2018. [Online]. Available: https://www.sciencedirect.com/science/article/pii/S0168900218311227

[64] B. Radics, D. J. Murtagh, Y. Yamazaki, and F. Robicheaux, "Scaling behavior of the ground-state antihydrogen yield as a function of positron density and temperature from classical-trajectory Monte Carlo simulations," *Physical Review A*, vol. 90, no. 3, p. 032704, Sep. 2014. [Online]. Available: http://link.aps.org/doi/10.1103/PhysRevA.90.032704

[65] E. Widmann and M. Hori, "ASACUSA STATUS REPORT Recent progress and plans for LS2," CERN, Geneva, Tech. Rep. CERN-SPSC-2019-006. SPSC-SR-245, Jan 2019. [Online]. Available: https://cds.cern.ch/record/2654222

[66] C. Amsler, D. Barna, H. Breuker, S. Chesnevskaya, G. Costantini, R. Ferragut, M. Giammarchi, A. Gligorova, H. Higaki, M. Hori, E. D. Hunter, Y. Kanai, V. Kletzl, V. Kraxberger, N. Kuroda, A. Lanz, M. Leali, V. Mäckel, G. Maero, C. Malbrunot, V. Mascagna, Y. Matsuda, S. Migliorati, D. J. Murtagh, Y. Nagata, A. Nanda, L. Nowak, E. Pasino, W. Pirkl, M. Romé, M. C. Simon, M. Tajima, V. Toso, S. Ulmer, U. Uggerhøj, L. Venturelli, A. Weiser, E. Widmann, T. Wolz, Y. Yamazaki, and J. Zmeskal, "Status report of the ASACUSA experiment - progress in 2020 and plans for 2021," CERN, Geneva, Tech. Rep., Jan 2021. [Online]. Available: https://cds.cern.ch/record/2748998

[67] T. Poikela, J. Plosila, T. Westerlund, M. Campbell, M. D. Gaspari, X. Llopart, V. Gromov, R. Kluit, M. van Beuzekom, F. Zappon, V. Zivkovic, C. Brezina, K. Desch, Y. Fu, and A. Kruth, "Timepix3: a 65k channel hybrid pixel readout chip with simultaneous ToA/ToT and sparse readout," *Journal of Instrumentation*, vol. 9, no. 05, p. C05013, 2014. [Online]. Available: https://doi.org/10.1088/1748-0221/9/05/C05013

[68] T. Böhlen, F. Cerutti, M. Chin, A. Fassò, A. Ferrari, P. Ortega, A. Mairani, P. Sala, G. Smirnov, and V. Vlachoudis, "The fluka code: Developments and challenges for high energy and medical applications," *Nuclear Data Sheets*, vol. 120, pp. 211 – 214, 2014. [Online]. Available: https://doi.org/10.1016/j.nds.2014.07.049

[69] A. Galoyan, A. Ribon, and V. Uzhinsky, "Dynamics of Anti-Proton–Protons and Anti-Proton–Nucleus Reactions," *Nucl. Theor.*, vol. 35, pp. 194–202, 2016.

[70] P. V. Degtyarenko, M. V. Kossov, and H.-P. Wellisch, "Chiral invariant phase space event generator," *The European Physical Journal A*, vol. 8, no. 2, pp. 217–222, Jul 2000. [Online]. Available: https://doi.org/10.1007/s100500070108

[71] A. Ferrari and P. R. Sala, "The physics of high energy reactions," CERN-ATL-PHYS-97-113, Tech. Rep., 1997.

[72] T. Campbell-Ricketts, M. Kroupa, and L. Pinsky, "Spectroscopy of high-energy ions with timepix3," *Journal of Instrumentation*, vol. 11, no. 11, pp. P11 007–P11 007, nov 2016. [Online]. Available: https://doi.org/10.10882F1748-02212F112F112Fp11007

[73] S. Spannagel, K. Wolters, D. Hynds, N. Alipour Tehrani, M. Benoit, D. Dannheim, N. Gauvin, A. Nürnberg, P. Schütze, and M. Vicente, "Allpix2: A modular simulation framework for silicon detectors," *Nucl. Instrum. Meth. A*, vol. 901, pp. 164 – 172, 2018. [Online]. Available: https://doi.org/10.1016/j.nima.2018.06.020

[74] A. Boudard, J. Cugnon, J.-C. David, S. Leray, and D. Mancusi, "New potentialities of the Liège intranuclear cascade model for reactions induced by nucleons and light charged particles," *Phys. Rev. C*, vol. 87, p. 014606, Jan 2013. [Online]. Available: https://link.aps.org/doi/10.1103/PhysRevC.87.014606

[75] S. Kirkpatrick, C. D. Gelatt, and M. P. Vecchi, "Optimization by simulated annealing," *Science*, vol. 220, no. 4598, pp. 671–680, 1983. [Online]. Available: https://www.science.org/doi/abs/10.1126/science.220.4598.671

[76] N. Kuroda, H. A. Torii, M. Shibata, Y. Nagata, D. Barna, M. Hori, D. Horváth, A. Mohri, J. Eades, K. Komaki, and Y. Yamazaki, "Radial compression of an antiproton cloud for production of intense antiproton beams," *Phys. Rev. Lett.*, vol. 100, p. 203402, May 2008. [Online]. Available: https://link.aps.org/doi/10.1103/PhysRevLett.100.203402

[77] H. A. Torii, N. Kuroda, M. Shibata, Y. Nagata, D. Barna, M. Hori, A. Mohri, K. Komaki, and Y. Yamazaki, "Extraction of ultra-slow antiproton beams and their physics application," *AIP Conference Proceedings*, vol. 796, no. 1, pp. 413–416, 2005. [Online]. Available: https://aip.scitation.org/doi/abs/10.1063/1.2130204

[78] G. Sikler, "Massenspektrometrie kurzlebiger Sr- und Sn-isotope und Aufbau der SHIPTRAP-Penningfallen," Ph.D. dissertation, Universität Heidelberg, 2003. [Online]. Available: http://www.ub.uni-heidelberg.de/archiv/3397

[79] A. Bianconi, M. Corradini, A. Cristiano, M. Leali, E. Lodi Rizzini, L. Venturelli, N. Zurlo, and R. Donà, "Experimental evidence of antiproton reflection by a solid surface," *Phys. Rev. A*, vol. 78, p. 022506, Aug 2008. [Online]. Available: https://link.aps.org/doi/10.1103/PhysRevA.78.022506

[80] M. Diermaier, C. B. Jepsen, B. Kolbinger, C. Malbrunot, O. Massiczek, C. Sauerzopf, M. C. Simon, J. Zmeskal, and E. Widmann, "In-beam measurement of the hydrogen hyperfine splitting and prospects for antihydrogen spectroscopy," *Nat Commun*, vol. 8, Jun. 2017.

[81] C. Malbrunot, C. Amsler, S. A. Cuendis, H. Breuker, P. Dupre, M. Fleck, H. Higaki, Y. Kanai, B. Kolbinger, N. Kuroda, M. Leali, V. Mäckel, V. Mascagna, O. Massiczek, Y. Matsuda, Y. Nagata, M. C. Simon, H. Spitzer, M. Tajima, S. Ulmer, L. Venturelli, E. Widmann, M. Wiesinger, Y. Yamazaki, and J. Zmeskal, *Phil. Trans. R. Soc. A*, vol. 376, no. 2116, p. 20170273, Mar. 2018.

[82] E. Widmann *et al.*, "Hyperfine spectroscopy of hydrogen and antihydrogen in ASACUSA," *Hyperfine Interact*, vol. 240, p. 5, 2019. [Online]. Available: https://doi.org/10.1007/s10751-018-1536-9

[83] E. Widmann, "In-beam hyperfine spectroscopy of antihydrogen, hydrogen and deuterium," in *9th Meeting on CPT and Lorentz Symmetry*, 12 2022.

[84] C. Malbrunot, M. Diermaier, M. Simon, C. Amsler, S. A. Cuendis, H. Breuker, C. Evans, M. Fleck, B. Kolbinger, A. Lanz, M. Leali, V. Maeckel, V. Mascagna, O. Massiczek, Y. Matsuda, Y. Nagata, C. Sauerzopf, L. Venturelli, E. Widmann, M. Wiesinger, Y. Yamazaki, and J. Zmeskal, "A hydrogen beam to characterize the asacusa antihydrogen hyperfine spectrometer," *Nuclear Instruments and Methods in Physics Research Section A: Accelerators, Spectrometers, Detectors and Associated Equipment*, vol. 935, pp. 110 – 120, 2019. [Online]. Available: http://www.sciencedirect.com/science/article/pii/S0168900219305315

[85] M. A. Humphrey, D. F. Phillips, E. M. Mattison, R. F. C. Vessot, R. E. Stoner, and R. L. Walsworth, "Testing CPT and Lorentz symmetry with hydrogen masers," *Physical Review A - Atomic, Molecular, and Optical Physics*, vol. 68, no. 6, pp. 063 807/1–063 807/14, 2003.

[86] R. Lundmark, C. Malbrunot, Y. Nagata, B. Radics, C. Sauerzopf, and E. Widmann, *J. Phys. B: At. Mol. Opt. Phys.*, vol. 48, no. 18, p. 184001, 2015.

[87] T. Wolz, C. Malbrunot, M. Vieille-Grosjean, and D. Comparat, "Stimulated decay and formation of antihydrogen atoms," *Phys. Rev. A*, vol. 101, p. 043412, Apr 2020. [Online]. Available: https://link.aps.org/doi/10.1103/PhysRevA.101.043412

[88] D. Comparat and C. Malbrunot, "Laser-stimulated deexcitation of rydberg antihydrogen atoms," *Phys. Rev. A*, vol. 99, p. 013418, Jan 2019. [Online]. Available: https://link.aps.org/doi/10.1103/PhysRevA.99.013418

[89] M. Vieille-Grosjean, E. Dimova, Z. Mazzotta, D. Comparat, T. Wolz, and C. L. S. Malbrunot, "Induced THz transitions in Rydberg caesium atoms for application in antihydrogen experiments," *The European Physical Journal D*, vol. 75, no. 1, p. 27, 2021.

[90] T. Wolz, "Controlled manipulation of atoms in rydberg quantum states for application in experiments with antihydrogen," Ph.D. dissertation, Technische Universität, Darmstadt, 2022, in press.

[91] V. Zhelyazkova and S. D. Hogan, "Preparation of circular rydberg states in helium using the crossed-fields method," *Phys. Rev. A*, vol. 94, p. 023415, Aug 2016. [Online]. Available: https://link.aps.org/doi/10.1103/PhysRevA.94.023415

[92] H. P. Garnir, Y. Baudinet-Robinet, P. D. Dumont, and A. El Himdy, "Measurement of the ratio of the 2s to the 2p populations for beam-foil excited hydrogen," *Zeitschrift für Physik D Atoms, Molecules and Clusters*, vol. 14, no. 1, pp. 45–49, 1989. [Online]. Available: https://doi.org/10.1007/BF01401342